Monthly Notices of the ROYAL ASTRONOMICAL SOCIETY

MNRAS **544,** 2698–2712 (2025) https://doi.org/10.1093/mnras/staf1816
Advance Access publication 2025 October 21

Probing the magneto-ionic medium of the Milky Way using pulsars

Saakshi Dhakal[1,2]★ and Amit Seta[2]★

[1]*Research School of Earth Sciences, Australian National University, Canberra, ACT 2601, Australia*
[2]*Research School of Astronomy and Astrophysics, Australian National University, Canberra, ACT 2611, Australia*

Accepted 2025 October 13. Received 2025 October 13; in original form 2025 January 19

ABSTRACT

Magnetic fields are fundamental to the dynamics of the interstellar medium (ISM) in spiral galaxies and are often separated into large-scale, regular ($\boldsymbol{B}$), and small-scale, random ($\boldsymbol{b}$) components. The thermal electron density, $n_{\rm e}$, can also be divided into large-scale, diffuse, $\langle n_{\rm e}\rangle$, and small-scale, clumpy, $\delta n_{\rm e}$, components. Estimating the properties of b and $\delta n_{\rm e}$ from observations, even within the Milky Way, has long been challenging. This work addresses the challenge using pulsars, which probe the Milky Way's magneto-ionic medium. Using data of more than 1200 pulsars from the Australia Telescope National Facility pulsar catalogue, we combine dispersion (DM) and rotation (RM) measures with theoretical models to estimate both small- and large-scale properties of the Galactic magnetic field and thermal electron density. We find no significant correlation between the average parallel magnetic field strength, $\langle B_{\parallel}\rangle(\mu{\rm G}) = 1.232\,{\rm RM\,(rad\,m^{-2})/DM\,(pc\,cm^{-3})}$, and pulsar distance. For pulsars within 20 kpc, we estimate $|B| \approx 1.2\,\mu$G and $\langle n_{\rm e}\rangle \approx 0.05\,{\rm cm^{-3}}$. More importantly, we determine correlation lengths of small-scale components, $\ell_b \approx 20$–30 pc and $\ell_{\delta n_{\rm e}} \approx 250$–$300$ pc. At smaller distances, B remains roughly constant, while $\langle n_{\rm e}\rangle$ increases and both length scales decrease. These results refine our understanding of fundamental scales in the magneto-ionic medium, aiding the interpretation of extragalactic RMs and providing insights into the role of magnetic fields in galaxies.

Key words: magnetic fields – plasmas – polarization – pulsars: general – ISM: magnetic fields – Galaxy: general.

1 INTRODUCTION

Understanding the magnetic fields in our Milky Way is essential for uncovering the astrophysical processes that shape its evolution. These fields play a pivotal role in regulating star formation (M. R. Krumholz & C. Federrath 2019; K. Pattle et al. 2023), guiding cosmic-ray propagation (A. Shukurov et al. 2017; M. Ruszkowski & C. Pfrommer 2023), and driving the dynamics of the interstellar gas (R. Shetty & E. C. Ostriker 2006; Planck Collaboration XIII 2016).

Several observational probes are used to trace the magnetic fields within the interstellar medium (ISM) of galaxies: optical polarization, Zeeman splitting of spectral lines, polarized emission from dust and molecules, polarized synchrotron emission, and Faraday rotation (U. Klein & A. Fletcher 2015). In general, each probe is useful for probing different regions or phases of the ISM. For example, Faraday rotation probes the magnetic field in the diffuse, ionized ISM, while dust polarization or Zeeman effect probes the colder, denser ISM (K. Ferrière 2020; S. Martin-Alvarez et al. 2024; A. Seta & N. M. McClure-Griffiths 2025).

Observationally, magnetic fields in spiral galaxies are divided into large-scale, regular (on scales of a few kpc) and small-scale, random (on scales of $\lesssim 100$ pc) components (R. Beck et al. 1996; A. Brandenburg & K. Subramanian 2005; R. Beck 2016; F. Rincon 2019; A. Shukurov & K. Subramanian 2021). Similarly, the thermal electron density is also divided into large-scale, diffuse (on scales of 1–2 kpc) and small-scale, clumpy (on scales of a 10–100 pc, roughly comparable to the size of H II regions) components (J. R. Jokipii & I. Lerche 1969; J. W. Hartman et al. 1997; B. M. Gaensler et al. 2008; B. D. Savage & B. P. Wakker 2009; M. Azimlu, P. Barmby & R. Marciniak 2011; D. I. Jones, Igoshev & Haverkorn 2016).

Despite the established importance of magnetic fields, uncertainties persist regarding their exact role in galactic evolution, primarily due to observational challenges in measuring field properties on smaller scales. This work aims to address these uncertainties by leveraging pulsar observations to refine our understanding of the Milky Way's magneto-ionic medium, focusing on the length scale of the small-scale magnetic fields and thermal electron densities.

Pulsars serve as ideal probes of the Galaxy's magneto-ionic medium (D. R. Lorimer & M. Kramer 2012) since they provide dispersion and Faraday rotation measures, DM and RM, which can be used to determine properties of both the thermal electron density and magnetic fields. For our analysis, we use DM, RM, and distance to the pulsar, L, from the Australian Telescope National Facility (ATNF) Pulsar Catalogue (R. N. Manchester et al. 2005, version 2.4.0). Their widespread distribution across the Milky Way offers great coverage of diverse Galactic environments (R. J. Rand & S. R. Kulkarni 1989; J. L. Han et al. 2018). Although pulsar-based measurements face challenges, particularly with distance estimation (J. P. W. Verbiest et al. 2012; R. Jansson & G. R. Farrar 2012; A. Moran et al. 2023; K. I. I. Koljonen et al. 2024; S. K. Ocker et al. 2024), they remain crucial for mapping the magneto-ionic medium. Here, we first describe RM and DM (Section 1.1) and then the method to determine the average magnetic field strength along the pulsar sightline from RM and DM (Section 1.2).

★ E-mail: saakshidhakal46@gmail.com (SD), amit.seta@anu.edu.au (AS)

1.1 RM and DM from pulsars

The dispersion measure (DM) of a pulsar is derived from the broadening of the observed pulse across a finite bandwidth. Physically, it represents the integral of the thermal electron density, n_e, along the line of sight from the pulsar to the observer (A. Hewish et al. 1968):

$$\frac{\mathrm{DM}}{1\ \mathrm{pc\ cm^{-3}}} = \int_L \frac{n_e}{1\ \mathrm{cm^{-3}}} \frac{\mathrm{d}l}{1\ \mathrm{pc}}, \tag{1}$$

where L is the total path length or equivalently the distance to the pulsar.

The rotation measure (RM) quantifies the change in the polarization angle, $\Delta\theta$, as light passes through the ISM:

$$\frac{\Delta\theta}{1\ \mathrm{rad}} = \frac{\mathrm{RM}}{1\ \mathrm{rad\ m^{-2}}} \frac{\lambda^2}{1\ \mathrm{m^2}}, \tag{2}$$

where λ is the wavelength and RM is expressed as:

$$\frac{\mathrm{RM}}{1\ \mathrm{rad\ m^{-2}}} = 0.812 \int_L \frac{n_e}{1\ \mathrm{cm^{-3}}} \frac{B_\parallel}{1\ \mu\mathrm{G}} \frac{\mathrm{d}l}{1\ \mathrm{pc}}, \tag{3}$$

where $B_\parallel$ is the component of the magnetic field parallel to the line of sight. By combining RM and DM, we can study the properties of the ISM and map magnetic fields in the Milky Way (e.g. M. Haverkorn 2015; J. L. Han 2017; Y. K. Ma et al. 2020).

1.2 Estimating average magnetic fields from RM and DM

By using both RM and DM from pulsars observations, we can estimate the properties of magnetic fields within the Milky Way (F. G. Smith 1968; R. N. Manchester 1972, 1974; A. G. Lyne & F. G. Smith 1989; R. J. Rand & S. R. Kulkarni 1989; C. Indrani & A. A. Deshpande 1999; J. L. Han, R. N. Manchester & G. J. Qiao 1999; D. Mitra et al. 2003; J. L. Han et al. 2006, 2018; C. Sobey et al. 2019; A. Seta & C. Federrath 2021b; C. P. Lee et al. 2024)[1]

The average magnetic field along the line of sight, $\langle B_\parallel \rangle$, can be estimated as

$$\frac{\langle B_\parallel \rangle}{1\ \mu\mathrm{G}} = \frac{\int_L \frac{n_e}{1\ \mathrm{cm^{-3}}} \frac{B_\parallel}{1\ \mu\mathrm{G}} \frac{\mathrm{d}l}{1\ \mathrm{pc}}}{\int_L \frac{n_e}{1\ \mathrm{cm^{-3}}} \frac{\mathrm{d}l}{1\ \mathrm{pc}}} = 1.232 \frac{\mathrm{RM}\ /\ [1\ \mathrm{rad\ m^{-2}}]}{\mathrm{DM}\ /\ [1\ \mathrm{pc\ cm^{-3}}]}. \tag{4}$$

This equation assumes that the thermal electron density (n_e) and the magnetic field ($B_\parallel$) are uncorrelated. If a correlation (or anticorrelation) exists, it could lead to an overestimation (or underestimation) of $\langle B_\parallel \rangle$ (R. Beck et al. 2003). Over large path lengths (on the order of kiloparsecs), this assumption has been shown to hold true (A. Seta & C. Federrath 2021b). The effect of such a correlation (or anticorrelation) on smaller scales might exist and can be included as a correction factor (R. Beck et al. 2003; A. Shukurov & K. Subramanian 2021) but given that most pulsars are located at such large distances, we expect the effect to be negligible (consistent with A. Seta & C. Federrath 2021b).

Estimating the magnetic field strength along the line of sight requires knowledge of both the path length (i.e. the distance to the pulsar) and the scales over which the magnetic field varies. However, pulsar distances are often estimated indirectly via DM values, which rely on models of the Galaxy's thermal electron density distribution. It is also often very hard to estimate the magnetic field length scale, especially for the small-scale magnetic field, which this work aims to determine.

The primary models used to estimate pulsar distances are NE2001 (J. M. Cordes & T. J. W. Lazio 2002) and YMW16 (J. M. Yao et al. 2017). Here, these DM-based distance estimates are referred to as $\mathrm{L_{DM}}$. The ATNF pulsar catalogue (R. N. Manchester et al. 2005) primarily uses the YMW16 model (J. M. Yao et al. 2017) for $\langle n_e \rangle$, which, despite being derived from DM measurements, carries inherent uncertainties (J. P. W. Verbiest et al. 2012; A. Moran et al. 2023). This creates a circularity issue; the electron density model is constructed using DM values, which are then used to estimate pulsar distances. To mitigate this, the catalogue also includes independently determined distances for about 250 pulsars based on parallax measurements (R. N. Manchester et al. 2005, version 2.4.0: https://www.atnf.csiro.au/research/pulsar/psrcat). These independently determined distances are referred to as $\mathrm{L_{Ind}}$.

Our approach extends further and diverges from previous studies by simultaneously analysing small- and large-scale thermal electron densities and magnetic fields. Our goal is to ascertain not only their strengths but also the length scale of their small-scale components, ℓ_b and $\ell_{\delta n_e}$. We adopt and modify a method based on the approach outlined in section IV.2. of A. A. Ruzmaikin, D. D. Sokoloff & A. M. Shukurov (1988).

The rest of the paper is organized as follows. In Section 2, we describe our methodology and our results are presented in Section 3. In Section 4, we discuss our results, their implications, and the assumptions of the study. Finally, we summarize our work and conclude in Section 5.

2 METHODOLOGY

2.1 Analysis of pulsar RMs

As briefly discussed before, the total magnetic field in galaxies, $\boldsymbol{B}_{\mathrm{tot}}$, can be divided into two components (see A. Seta & C. Federrath 2024, for a method to separate the two components from RM observations): the large-scale component, which is coherent over kiloparsec scales ($\boldsymbol{B}$) and the small-scale, random component, which varies over much smaller scales ($\boldsymbol{b}$). The total magnetic field in galaxies can be written as,

$$\boldsymbol{B}_{\mathrm{tot}} = \boldsymbol{B} + \boldsymbol{b}. \tag{5}$$

Here, we assume that the large- and small-scale magnetic field components are statistically independent of each other. We note that the small-scale component $\boldsymbol{b}$ can be correlated with the large-scale field $\boldsymbol{B}$ because turbulence also tangles the large-scale field to generate small-scale random fluctuations (J. F. Hollins et al. 2017; A. Seta & C. Federrath 2020; A. Shukurov & K. Subramanian 2021). In our analysis, however, we treat $\boldsymbol{B}$ and $\boldsymbol{b}$ as statistically independent as it allows a tractable separation of their contributions to RM. Given the lack of analytical prescription for the $\boldsymbol{B}$-$\boldsymbol{b}$ correlation due to the tangling of the large-scale field, we neglect the contribution it may introduce.

To analyse the connection of these components individually with the observable, RM, we multiply both sides of equation (5) by the thermal electron density (n_e) and then take the projection along the line of sight as,

$$n_e B_{\mathrm{tot},\parallel} = n_e B_\parallel + n_e b_\parallel. \tag{6}$$

[1]Fast Radio Bursts (FRBs) can similarly be used to estimate extragalactic magnetic fields using their RM and DM values (T. Akahori, D. Ryu & B. M. Gaensler 2016; V. Ravi et al. 2016; J. X. Prochaska et al. 2019; S. Hackstein et al. 2019).

To compute RM, we integrate both sides of equation () over the path length, L (here, equal to the distance to pulsar) as,

$$\int_L n_e B_{\mathrm{tot},\parallel} \mathrm{d}l = \int_L n_e B_\parallel \mathrm{d}l + \int_L n_e b_\parallel \mathrm{d}l, \tag{7}$$

where $B_\parallel$ is the parallel (line-of-sight) component of the large-scale field and $b_\parallel$ is the parallel component of the small-scale field, which gives,

$$\mathrm{RM} = \mathrm{RM}_{\boldsymbol{B}} + \mathrm{RM}_{\boldsymbol{b}}, \tag{8}$$

where RM represents the observed RM associated with the total magnetic field and $\mathrm{RM}_{\boldsymbol{B}}$ and $\mathrm{RM}_{\boldsymbol{b}}$ represents that for each component.

Adopting a simple model from section IV.2. of A. A. Ruzmaikin et al. (1988), the contribution of the large-scale magnetic field for a single point source like a pulsar is expressed as,

$$\mathrm{RM}_{\boldsymbol{B}} = 0.812\, B\, \langle n_e \rangle\, L\, \cos\left(\tfrac{\boldsymbol{B}\cdot\boldsymbol{L}}{BL}\right), \tag{9}$$

$$= c_0\, L\, [\cos(\mathrm{Gb}_0)\cos(\mathrm{Gb})\cos(\mathrm{Gl}-\mathrm{Gl}_0) + \sin(\mathrm{Gb}_0)\sin(\mathrm{Gb})], \tag{10}$$

where $\langle n_e \rangle$ is the mean electron density along the line of sight, L is the distance to the pulsar, $\boldsymbol{L}$ is the vector joining the location of the pulsar to us. The term c_0 is defined as $0.812\,\langle n_e \rangle\, B$. The galactic coordinates, Gl and Gb, represent the pulsar's position in the Galaxy, while Gl_0 and Gb_0 are coordinate reference parameters for the large-scale magnetic field model. We note that this is an unidirectional model with direction $(\mathrm{Gl}_0, \mathrm{Gb}_0)$ and thus we primarily focus on the magnitude of the estimated large-scale field, $|B|$, for our results. We also know that there is at least one large-scale magnetic field reversal near the Sagittarius spiral arm in the first Galactic quadrant (X. H. Sun et al. 2008; C. L. Van Eck et al. 2011; R. Jansson & G. R. Farrar 2012; A. Ordog et al. 2017; J. L. Han et al. 2018) and the possible effects of this and potentially other reversals are discussed in Sections 3.6 and 4.4.

We further note that, after adopting a model for the large-scale magnetic field, a perturbation-type analysis assuming the effect of the small-scale field as a weak perturbation to the large-scale field is not valid, since the observed strengths of the small-scale magnetic field, $|\boldsymbol{b}|$, are typically comparable to or even exceed those of the large-scale field, $|\boldsymbol{B}|$ (M. Haverkorn 2015; R. Beck 2016).

To proceed with the statistical analysis, we first examine the mean of RM, denoted $\langle \mathrm{RM} \rangle$. The mean of the total field can be expressed as the sum of the large- and small-scale contributions,

$$\langle \mathrm{RM} \rangle = \mathrm{RM}_{\boldsymbol{B}} + \langle \mathrm{RM}_{\boldsymbol{b}} \rangle, \tag{11}$$

where we have used that $\langle \mathrm{RM}_{\boldsymbol{B}} \rangle \approx \mathrm{RM}_{\boldsymbol{B}}$ (see equation 10).

Given that the length scale of the small-scale component is significantly smaller than the large-scale component and the distance to the pulsar (of the order of kpc) and assuming uncorrelated thermal electron density and magnetic fields, we can simplify (11) to

$$\langle \mathrm{RM}_{\boldsymbol{b}} \rangle \approx 0 \text{ and } \langle \mathrm{RM} \rangle \approx \mathrm{RM}_{\boldsymbol{B}}. \tag{12}$$

This implies that the total average RM is equal to the average RM of the large-scale field, as the small-scale contribution averages out to zero.

We continue our statistical analysis by determining the variance of RM or how much RM fluctuates. This is given by

$$\sigma^2(\mathrm{RM}) = \sigma^2(\mathrm{RM}_{\boldsymbol{B}}) + \sigma^2(\mathrm{RM}_{\boldsymbol{b}}). \tag{13}$$

Since most variations in RM along the line of sight are due to the small-scale, random magnetic field fluctuations,

$$\sigma^2(\mathrm{RM}_{\boldsymbol{B}}) \approx 0 \text{ and } \sigma^2(\mathrm{RM}) \approx \sigma^2(\mathrm{RM}_{\boldsymbol{b}}). \tag{14}$$

This implies that the RM fluctuations are primarily determined by the small-scale magnetic field fluctuations.

Now, we introduce the quantity,

$$\mathcal{P}(l) = n_e(l)\, (\boldsymbol{B}(l)\cdot\hat{L}), \tag{15}$$

where $\hat{L}$ represents the unit vector along the line of sight and l denotes distance along it from the pulsar. Using $\mathcal{P}(l)$, the mean and variance of RM can be written as

$$\langle \mathrm{RM} \rangle = 0.812 \int_L \mathcal{P}(l)\, \mathrm{d}l \tag{16}$$

and

$$\sigma^2(\mathrm{RM}) = (0.812)^2 \int_L \mathrm{d}l_1 \int_L \mathrm{d}l_2\, \left[\overline{\mathcal{P}(l_2)\mathcal{P}(l_2)} - \bar{\mathcal{P}}(l_1)\bar{\mathcal{P}}(l_2)\right]. \tag{17}$$

In equation (17), the overbars denote an ensemble or spatial average over realizations of the random magnetic field or electron density along a line of sight, while the angular brackets $\langle\cdot\rangle$ (e.g. in equation 12) denote a statistical or expected value. In practice, both averaging procedures are related, but we use overbars to indicate a local or sample-based mean and angular brackets to indicate a theoretical or global expectation value.

Assuming that the small-scale field is homogeneous, the quantity within the square bracket in equation (17) is a two-point correlation function $\mathcal{C}(l_1, l_2)$. This is a crucial assumption that allows the correlation function to depend only on the distance between two points (this is also directly related to structure functions, described in A. Seta et al. 2023),

$$s = |l_1 - l_2|. \tag{18}$$

After some algebra, equation (17) simplifies to,

$$\sigma^2(\mathrm{RM}) = 2\, {c_0}^2 \int_L (L-s)\, \mathcal{C}(s)\, \mathrm{d}s. \tag{19}$$

This analysis assumes the presence of a characteristic scale of the small-scale field, ℓ_b (the typical size over which the small-scale magnetic field remains correlated). When $s \ll \ell_b$, the values of $\mathcal{P}(s_1)$ and $\mathcal{P}(s_2)$ are strongly correlated, resulting in larger values of $\mathcal{C}(s)$. Conversely, for $s \gg \ell_b$, $\mathcal{P}(s_1)$ and $\mathcal{P}(s_2)$ become effectively uncorrelated, so that $\mathcal{C}(s) \to 0$. In physical terms, if two points along the line of sight are separated by a distance smaller than ℓ_b, the magnetic fields at those points are still related. If the distance between them is much larger than ℓ_b, the magnetic fields at those points no longer exhibit measurable correlation. We emphasize that here we are referring to the absence of correlation, which does not necessarily imply full statistical independence.

For a simple model, we assume correlation $\mathcal{C}(s)$ is represented by an exponential function,

$$\mathcal{C}(s) = \mathcal{C}_0 \exp(-s/\ell_b), \tag{20}$$

where $\mathcal{C}_0$ is a dimension-less constant. This correlation decays over a characteristic scale length, ℓ_b, which represents the typical size of magnetic field structures or the scale of small-scale magnetic fields. By adopting this exponential form, we can express the variance in RM (equation 17) that arises from small-scale magnetic fields (see Appendix A1 for the full derivation) as,

$$\sigma(\mathrm{RM}) = 2^{1/2}\, c_0\, {C_0}^{1/2}\, \ell_b \left[L/\ell_b - 1 + \exp(-L/\ell_b)\right]^{1/2}. \tag{21}$$

Now, since $\langle \mathrm{RM} \rangle \approx \mathrm{RM}_{\boldsymbol{B}}$ and $\sigma(\mathrm{RM}) \approx \sigma(\mathrm{RM}_{\boldsymbol{b}})$, using equations (10) and (21), for each pulsar, we model the total observed RM

as

$$\begin{aligned}\mathrm{RM} &= \mathrm{RM}_{\boldsymbol{B}} + \mathrm{RM}_{\boldsymbol{b}} \\ &= c_0 L[\cos(\mathrm{Gb}_0)\cos(\mathrm{Gb})\cos(\mathrm{Gl}-\mathrm{Gl}_0) \\ &\quad + \sin(\mathrm{Gb}_0)\sin(\mathrm{Gb})] + \left[L/\ell_b - 1 + \exp(-L/\ell_b)\right]^{1/2}\epsilon_{\mathrm{RM}},\end{aligned} \tag{22}$$

where ϵ_{RM} is a Gaussian random number picked from a distribution with mean zero and standard deviation $= 2^{1/2}\, c_0\, {C_0}^{1/2}\, \ell_b$ to capture the contribution from the small-scale magnetic fields to the total observed RM.

The observed value of RM is now parametrized using four values (c_0, Gl_0, Gb_0, and ℓ_b) of the modelled small- and large-scale magnetic fields. Note that with each RM value, the location (Gl and Gb) of and distance (L) to each pulsar are known in equation (22). Given a sample with N pulsars, to ensure $\langle \mathrm{RM}\rangle \approx \mathrm{RM}_{\boldsymbol{B}}$ and $\langle \mathrm{RM}\rangle_{\boldsymbol{b}} \approx 0$, we minimize the combined contribution of the sum of all ϵ_{RM}s added in Gaussian quadrature to the observed RM, $\mathcal{S}_{\mathrm{RM}}$, to determine the parameters, c_0, Gl_0, Gb_0, and ℓ_b, where $\mathcal{S}_{\mathrm{RM}}$ is given as,

$$\begin{aligned}\mathcal{S}_{\mathrm{RM}}\,(c_0, \mathrm{Gl}_0, \mathrm{Gb}_0, \ell_b) &= \frac{1}{\mathrm{N}}\sum_{i=1}^{\mathrm{N}} (\epsilon_{\mathrm{RM}})_i^2 \\ &= \frac{1}{\mathrm{N}}\sum_{i=1}^{\mathrm{N}} \left(\frac{\mathrm{RM}_i - \mathrm{RM}_{\boldsymbol{B},i}}{[L_i/\ell_b - 1 + \exp(-L_i/\ell_b)]^{1/2}}\right)^2,\end{aligned} \tag{23}$$

where RM_i and L_i are the observed RM of and distance to the ith pulsar in the sample with a total of N pulsars and $\mathrm{RM}_{\boldsymbol{B},i}$ is the contribution of the large-scale field for the ith pulsar computed using equation (10).

2.2 Analysis of pulsar DMs

Similar to the magnetic field decomposition, the thermal electron density can be separated into large- and small-scale components. The large-scale part, $\langle n_{\mathrm{e}}\rangle$, represents variations in the diffuse component varying over possibly larger kpc-sized ISM regions, while the small-scale fluctuations, δn_{e}, capture clumpy structures on scales of 10–100s of pc and probably also localized enhancements near H II regions (size of H II regions varies over a wide range, 10–200 pc, see M. Azimlu et al. 2011). This decomposition can be written as,

$$n_{\mathrm{e}} = \langle n_{\mathrm{e}}\rangle + \delta n_{\mathrm{e}}. \tag{24}$$

To compute the total DM we integrate both sides of equation (24) over the distance L to the pulsar as

$$\int_L n_{\mathrm{e}}\,\mathrm{d}l = \int_L \langle n_{\mathrm{e}}\rangle\,\mathrm{d}l + \int_L \delta n_{\mathrm{e}}\,\mathrm{d}l, \tag{25}$$

$$\mathrm{DM} = \mathrm{DM}_{\langle n_{\mathrm{e}}\rangle} + \mathrm{DM}_{\delta n_{\mathrm{e}}}. \tag{26}$$

Here, $\mathrm{DM}_{\langle n_{\mathrm{e}}\rangle}$ represents the contribution from the large-scale, diffuse component of the thermal electron density, while $\mathrm{DM}_{\delta n_{\mathrm{e}}}$ captures the contribution from small-scale fluctuations.

Like we did with the RMs, our statistical analysis of DM begins with their mean,

$$\langle \mathrm{DM}\rangle = \langle \mathrm{DM}_{\langle n_{\mathrm{e}}\rangle}\rangle + \langle \mathrm{DM}_{\delta n_{\mathrm{e}}}\rangle, \tag{27}$$

where $\langle \mathrm{DM}_{\langle n_{\mathrm{e}}\rangle}\rangle$ represents the mean contribution from large-scale thermal electron density structures and $\langle \mathrm{DM}_{\delta n_{\mathrm{e}}}\rangle$ represents the fluctuating contribution from small-scale thermal electron density. Again, we assume that $\langle \mathrm{DM}\rangle$ is primarily determined by $\langle \mathrm{DM}_{\delta n_{\mathrm{e}}}\rangle$, with $\langle \mathrm{DM}_{\delta n_{\mathrm{e}}}\rangle$ contributions being negligible in comparison (see J. R. Jokipii & I. Lerche 1969; G. Nelemans et al. 1997, for further discussion on this assumption). Thus,

$$\langle \mathrm{DM}_{\delta n_{\mathrm{e}}}\rangle \approx 0 \text{ and } \langle \mathrm{DM}\rangle \approx \langle \mathrm{DM}_{\langle n_{\mathrm{e}}\rangle}\rangle. \tag{28}$$

Furthermore,

$$\langle \mathrm{DM}_{\langle n_{\mathrm{e}}\rangle}\rangle = \langle n_{\mathrm{e}}\rangle\, L. \tag{29}$$

Then computing the variance gives

$$\sigma^2(\mathrm{DM}) = \sigma^2(\mathrm{DM}_{\langle n_{\mathrm{e}}\rangle}) + \sigma^2(\mathrm{DM}_{\delta n_{\mathrm{e}}}). \tag{30}$$

Assuming that the $\sigma^2(\mathrm{DM})$ is primarily due to the small-scale thermal electron density, we get

$$\sigma^2(\mathrm{DM}_{\langle n_{\mathrm{e}}\rangle}) \approx 0 \text{ and } \sigma^2(\mathrm{DM}) \approx \sigma^2(\mathrm{DM}_{\delta n_{\mathrm{e}}}). \tag{31}$$

The term $\sigma^2(\mathrm{DM}) \approx \sigma^2(\mathrm{DM}_{\delta n_{\mathrm{e}}})$ is now modelled below.

We now introduce,

$$\mathcal{Q}(l) = n_{\mathrm{e}}(l). \tag{32}$$

To model the total observed DM following the same approach as used for the RM analysis in Section 2.1, the variance of DM can be expressed as,

$$\sigma^2(\mathrm{DM}) = \int_L \mathrm{d}l_1 \int_L \mathrm{d}l_2 \left[\overline{\mathcal{Q}(l_1)\mathcal{Q}(l_2)} - \bar{\mathcal{Q}}(l_1)\bar{\mathcal{Q}}(l_2)\right]. \tag{33}$$

This can be further reduced in terms of the correlation function of the small-scale thermal electron density as,

$$\sigma^2(\mathrm{DM}) = 2\,\langle n_{\mathrm{e}}\rangle^2 \int_L (L-s)\,\mathcal{C}(s)\,\mathrm{d}s. \tag{34}$$

where $\mathcal{C}(s)$ represents the correlation function of the small-scale fluctuations. Assuming the familiar exponential decay for the correlation function,

$$\mathcal{C}(s) = \mathcal{C}_0 \exp(-s/\ell_{\delta n_{\mathrm{e}}}), \tag{35}$$

we obtain,

$$\sigma^2(\mathrm{DM}) = 2\,\langle n_{\mathrm{e}}\rangle^2 \left[L\ell_{\delta n_{\mathrm{e}}} + \ell_{\delta n_{\mathrm{e}}}^2\left(-1 + \exp(-L/\ell_{\delta n_{\mathrm{e}}})\right)\right], \tag{36}$$

which gives,

$$\sigma(\mathrm{DM}) = 2^{1/2}\, {C_0}^{1/2}\, \langle n_{\mathrm{e}}\rangle\, \ell_{\delta n_{\mathrm{e}}} \left[L/\ell_{\delta n_{\mathrm{e}}} - 1 + \exp(-L/\ell_{\delta n_{\mathrm{e}}})\right]^{1/2}. \tag{37}$$

Thus, using equations (29) and (37), the observed total DM is written as

$$\begin{aligned}\mathrm{DM} &= \mathrm{DM}_{\langle n_{\mathrm{e}}\rangle} + \sigma(\mathrm{DM}) \\ &= \langle n_{\mathrm{e}}\rangle\, L + \left[L/\ell_{\delta n_{\mathrm{e}}} - 1 + \exp(-L/\ell_{\delta n_{\mathrm{e}}})\right]^{1/2}\eta_{\mathrm{DM}},\end{aligned} \tag{38}$$

where η_{DM} is a Gaussian random number picked from a distribution with mean zero and standard deviation $= 2^{1/2}\, {C_0}^{1/2}\, \langle n_{\mathrm{e}}\rangle\, \ell_{\delta n_{\mathrm{e}}}$.

The observed DM for a pulsar at a distance L is parametrized using two values, $\langle n_{\mathrm{e}}\rangle$ and $\ell_{\delta n_{\mathrm{e}}}$, which are properties of the thermal electron density model. Given a sample of N pulsars, to ensure that we minimize the combined contribution of the sum of all η_{DM} added in Gaussian quadrature to the observed DM, $\mathcal{S}_{\mathrm{DM}}$, to determine the parameters, $\langle n_{\mathrm{e}}\rangle$ and $\ell_{\delta n_{\mathrm{e}}}$, where $\mathcal{S}_{\mathrm{DM}}$ is given as,

$$\begin{aligned}\mathcal{S}_{\mathrm{DM}}\,(\langle n_{\mathrm{e}}\rangle, \ell_{\delta n_{\mathrm{e}}}) &= \frac{1}{\mathrm{N}}\sum_{i=1}^{\mathrm{N}} (\eta_{\mathrm{DM}})_i^2 \\ &= \frac{1}{\mathrm{N}}\sum_{i=1}^{\mathrm{N}} \left(\frac{\mathrm{DM}_i - \mathrm{DM}_{\langle n_{\mathrm{e}}\rangle,i}}{[L_i/\ell_{\delta n_{\mathrm{e}}} - 1 + \exp(-L_i/\ell_{\delta n_{\mathrm{e}}})]^{1/2}}\right)^2,\end{aligned} \tag{39}$$

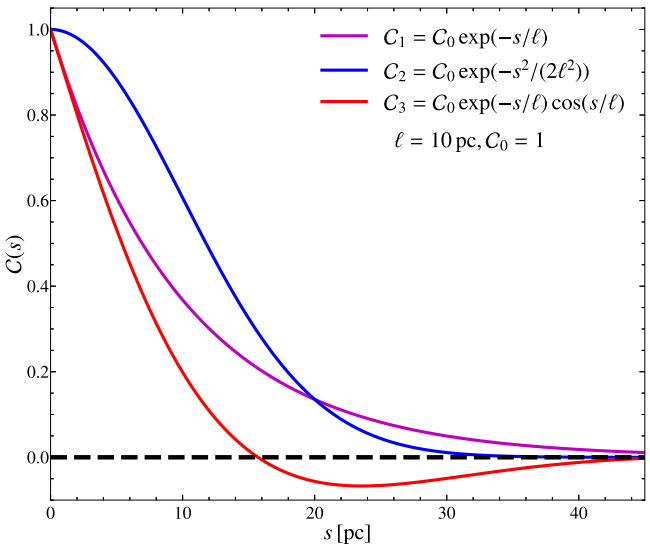

Figure 1. Comparison of three different correlation functions, $\mathcal{C}_1$, $\mathcal{C}_2$, and $\mathcal{C}_3$ (forms in the legend), as functions of the separation distance, s, in pc with a characteristic scale length, $\ell = 10$ pc and the dimensionless constant, $\mathcal{C}_0 = 1$. All the correlation functions start from 1 at $s = 0$ and approach 0 (dashed, black line) as $s \to \infty$. $\mathcal{C}_2$ goes to zero at a smaller separation than $\mathcal{C}_1$ and $\mathcal{C}_3$ allows the correlation to be negative before approaching zero. This illustrates the distinct behaviours of each correlation function at different separation distances, emphasizing their functional forms, relative amplitudes, and decay rates (see Section 2.3 for further discussion on differences).

where DM_i and L_i are the observed DM of and distance to the ith pulsar in the sample, respectively. $\mathrm{DM}_{\langle n_e\rangle,i}$ represents the large-scale thermal electron density contribution to the DM for the ith pulsar, DM_i, which is calculated using equation (29).

2.3 Correlation functions

One of the crucial assumptions in our statistical analysis is the choice of the correlation function for the small-scale components, b and δn_e. Though A. A. Ruzmaikin et al. (1988) used only an exponentially decaying function (e.g. equation 20), motivated by magnetic field correlation functions obtained from the results of turbulent magnetohydrodynamic simulations of the ISM (J. F. Hollins et al. 2017), we use the following three correlation functions for both the RM and DM analysis,

$$\begin{aligned}\mathcal{C}_1(s) &= \mathcal{C}_0 \exp(-s/\ell),\\ \mathcal{C}_2(s) &= \mathcal{C}_0 \exp(-s^2/(2\ell^2)),\\ \mathcal{C}_3(s) &= \mathcal{C}_0 \exp(-s/\ell)\cos(s/\ell),\end{aligned} \tag{40}$$

where s denotes separation (equation 18), ℓ is the characteristic length scale (either ℓ_b or $\ell_{\delta n_e}$), and $\mathcal{C}_0$ is a dimension-less constant. For a typical length scale, $\ell = 10$ pc, Fig. 1 shows how all three correlation functions depend on the separation, s.

For all three cases, the correlation is high at smaller separations and goes to zero at large separations, but the differences capture possible expected variations in the ISM (see J. F. Hollins et al. 2017, for further details). For example, the first two functions are decaying but $\mathcal{C}_2$ decays faster than $\mathcal{C}_1$ (compare blue and red lines in Fig. 1). Also, $\mathcal{C}_1$ and $\mathcal{C}_2$ model simple attenuation with separation, while the combination of an exponential decay with a cosine term in $\mathcal{C}_3$ allows the correlation to be negative and still bounce back to zero at larger distances. This anticorrelation in $\mathcal{C}_3$ can arise naturally from the solenoidal property of magnetic fields (see section 8.IV in Y. Zeldovich et al. 1986). Furthermore, for $\mathcal{C}_3$, the same scale is used in both the exponential and cosine terms. This scale is close to the correlation length of the random fields and, for the magnetic fields, this form of the correlation function assumes that typical field lines close within one correlation length. Such an approach provides a potentially more flexible representation of the small-scale components, enhancing our ability to model the complexities expected in the magnetic fields and thermal electron density distributions.

For each correlation function, the expressions used to compute the residual sums, $\mathcal{S}_{\mathrm{RM}}$ (equation 23) and $\mathcal{S}_{\mathrm{DM}}$ (equation 39), are derived analytically in Appendix A. Importantly, the last term in the denominator of these expressions, which reflects the contribution of the small-scale fluctuations, is explicitly modified depending on the chosen correlation function. This ensures that $\mathcal{S}_{\mathrm{RM}}$ and $\mathcal{S}_{\mathrm{DM}}$ correctly account for the different functional forms, whether $\mathcal{C}_1$, $\mathcal{C}_2$, or $\mathcal{C}_3$. Our method remains fully analytical up to this point, which also motivates the choice of these three correlation functions, as each allows for a closed-form expression suitable for residual sums and subsequent numerical minimization (described in the next subsection).

2.4 Minimization

Assuming various possible values of ℓ_b and observational data for 27 pulsars, A. A. Ruzmaikin et al. (1988) used analytical minimization for parameters Gl_0 (assuming $\mathrm{Gb}_0 = 0^\circ$), $\langle n_e\rangle$, and B. For our analysis, we use the `LMFIT` library (M. Newville et al. 2015) for numerical minimization (including non-linear methods). In Appendix B, we replicated their work on the original data set using our method. Here, we expand the method using our larger data set (N $\sim$ 3000 for DM and N $\sim$ 1300 for RM), extending minimization to include all parameters (Gl_0, Gb_0, $\langle n_e\rangle$, B, $\ell_{\delta n_e}$, and ℓ_b) and for all three correlation functions given in Section 2.3.

However, this approach yielded an excessively low reduced chi-squared value ($\chi^2 \ll 1$), indicating overfitting. Adjustments with varying correlation functions (Section 2.3) did not improve χ^2 significantly, suggesting that our data set size may not yet support the full parameter set. Thus, we fixed ℓ_b and $\ell_{\delta n_e}$ at pre-defined scales, iterating over ℓ values from 0.1 pc to 1 kpc as

$$\ell\,[\mathrm{pc}] = [0.1, 1, 5, 10, 15, 20, 25, 30, 50, 100, 200, 250, 500, 1000].$$

For each ℓ, we applied numerical least-squares minimization for Gl_0, Gb_0, $\langle n_e\rangle$, and B, assessing fit quality with χ^2. Then we interpolated χ^2 to refine ℓ_b and $\ell_{\delta n_e}$ estimates, identifying scales where χ^2 approaches 1, optimizing Gl_0, Gb_0, $\langle n_e\rangle$, and B.

To quantify uncertainties, we employed a Monte Carlo-type approach, perturbing RM and DM data up to 30 000 times based on observational errors ($\mathrm{RM}_{\mathrm{ERR}}$ and $\mathrm{DM}_{\mathrm{ERR}}$) and distance uncertainties (if available). Each perturbed data set was fit and parameter uncertainties were estimated as the difference between the 84th and 16th percentiles.

2.5 Data

The data for this work was sourced from the ATNF pulsar catalogue (R. N. Manchester et al. 2005, version 2.4.0, https://www.atnf.csiro.au/research/pulsar/psrcat). We restricted the data set to pulsars within the Milky Way, specifically those with distances ≤ 20 kpc. The primary parameters of interest include:

(i) Gl: Galactic longitude ($^\circ$)
(ii) Gb: Galactic latitude ($^\circ$)
(iii) RM: Rotation measure (rad m^{-2})

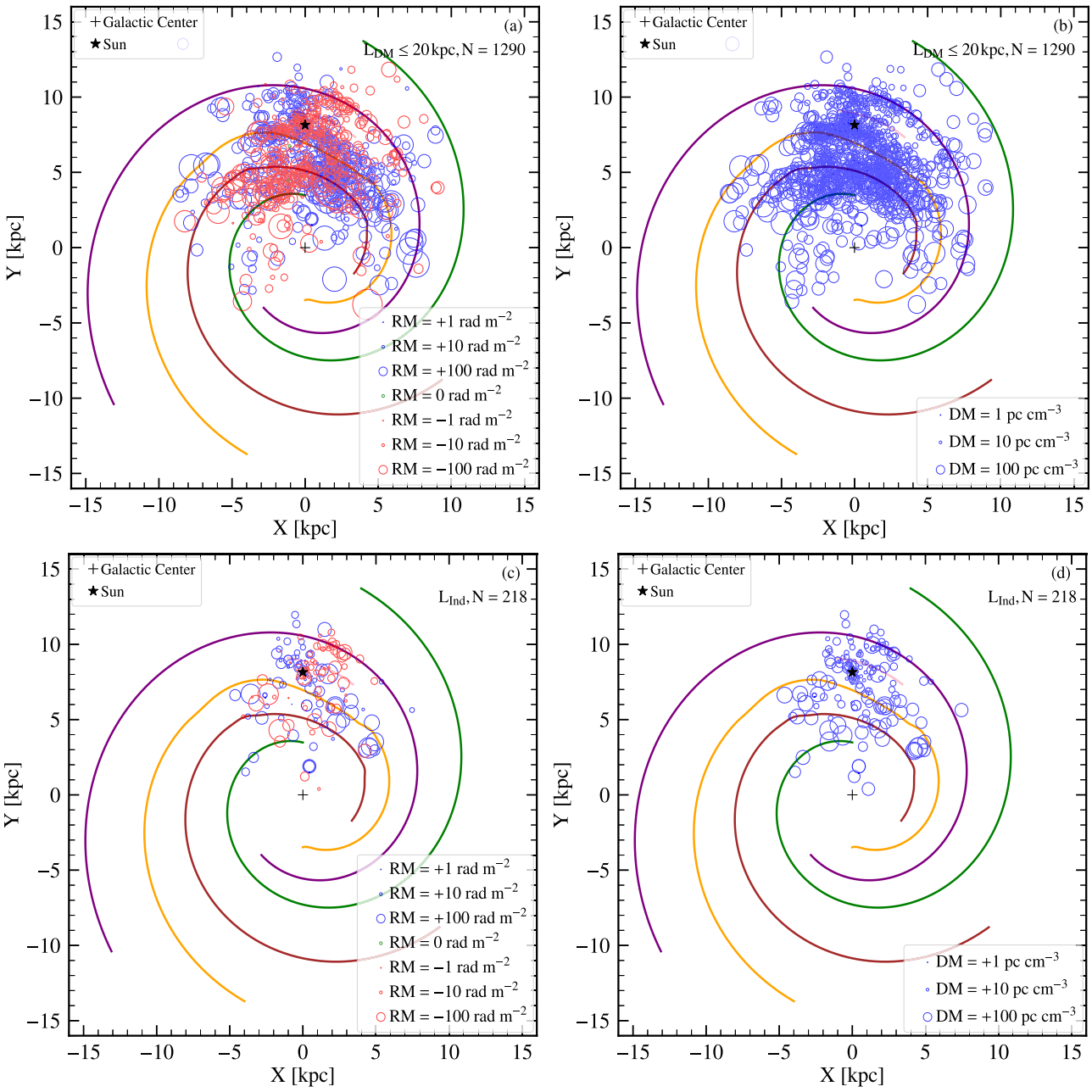

Figure 2. Pulsar data, RM (a, c) and DM (b, d), for both data sets, $L_{DM} \leq 20$ kpc (a, b) and L_{Ind} (c, d) with spiral arm model used in the NE2001 thermal electron density model (J. M. Cordes & T. J. W. Lazio 2002). As expected, most detected pulsars are concentrated around the Sun and thus the surrounding area is more sampled by the data. Our statistical analysis is, by extension, probing those regions more compared to the other parts of the Milky Way.

(iv) DM: Dispersion measure (pc cm^{-3})
(v) L_{DM}: Distance to the pulsar based on the electron density model by J. M. Yao et al. (2017) (kpc)
(vi) L_{Ind}: Independently determined distance to the pulsar (kpc)

The data set includes 3077 entries with both DM and L_{DM} values, while RM measurements are available only for 1290 pulsars. The subset of pulsars with independent distance estimates (L_{Ind}) includes 375 entries with DM values and 218 of these have RM values. It is also important to note that the parameters RM, DM, and L_{Ind} have symmetric errors associated with them [we note that L_{Ind} might have asymmetric errors for some of the pulsars, see A. T. Deller et al. (2019), but they are currently not included in the version 2.4.0 of the ATNF pulsar catalogue], while the relative errors in Gl and Gb computed from corresponding right ascension and declination are negligible, and L_{DM} do not have any reported errors in the data set.

3 RESULTS

3.1 Distribution of data

3.1.1 Pulsar distribution with spiral arms

Fig. 2 shows the distribution of pulsar data with spiral arms taken from the model used in the NE2001 thermal electron density model (J. M. Cordes & T. J. W. Lazio 2002). Most pulsars lie closer to the

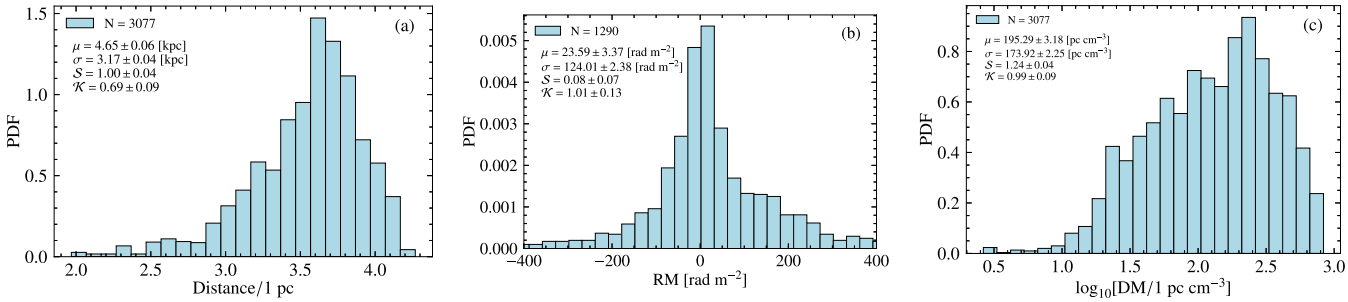

Figure 3. Distribution of data for RM, DM, and L_{DM}. Panels (a), (b), and (c) illustrate the histograms of RM, DM, and L_{DM}, respectively. All distributions observe moderate skewness except (b), which is more symmetric. In all figures, we also observe a $\mathcal{K} > 0$, suggesting that the data exhibits features of a non-normal distribution.

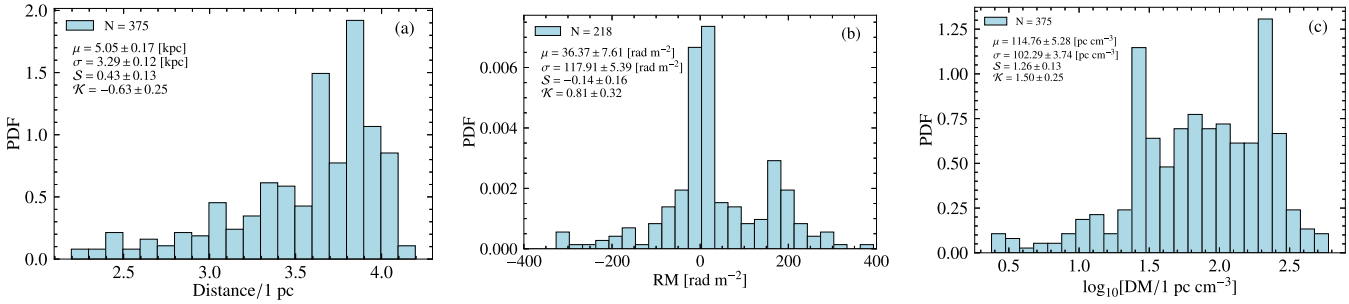

Figure 4. Same as Fig. 3 but for L_{Ind}. Here too, except RM, both distributions show skewness ($\mathcal{S}$). Based on the computed kurtosis ($\mathcal{K}$), all distributions show non-normal traits (note the negative $\mathcal{K}$ for L_{Ind}, which is probably due to a smaller number of samples in the histogram).

Sun and thus our statistical analysis, detailed in Section 2, is more sensitive to this part of the Milky Way compared to others. We also note that some of the distances in the L_{DM} sample can actually be incorrect and some of the pulsars can be closer than given by L_{DM} (K. I. I. Koljonen et al. 2024; S. K. Ocker et al. 2024). This is also the reason we perform a parallel analysis with the L_{Ind} sample but there the sample size is significantly smaller (by a factor of ≈ 6) compared to the L_{DM} sample and the L_{Ind} data set has even sparser sampling as seen in Figs. 2(c) and (d). Thus, for completeness, we provide and discuss results for both samples.

3.1.2 *Distance distribution:* L_{DM} *and* L_{Ind}

Figs. 3(a) and 4(a) present histograms for the data sets L_{DM} and L_{Ind}, respectively. The mean value for L_{DM} is measured at (4.65 ± 0.06) kpc, with a standard deviation of (3.17 ± 0.04) kpc. In contrast, L_{Ind} exhibits a higher mean of (5.05 ± 0.17) kpc, accompanied by a relatively larger error and a standard deviation of (3.29 ± 0.12) kpc. To further analyse the distributions, we calculated skewness ($\mathcal{S}$) and kurtosis ($\mathcal{K}$). High skewness is indicated by $|\mathcal{S}| > 1$, moderate skewness by $0.5 < |\mathcal{S}| \leq 1$, and approximate symmetry by $|\mathcal{S}| \leq 0.5$. A $\mathcal{K}$ near 0 suggests a Gaussian distribution, while values above 0 indicate non-Gaussian distributions with heavy tails.

For the L_{DM} data set, we observe moderate $\mathcal{S}$ and non-normal behaviour with $\mathcal{K} > 0$, suggesting that the distribution deviates from normality. In contrast, the L_{Ind} data set shows an approximately symmetrical distribution ($\mathcal{S} < 0.5$) but also exhibits non-normal characteristics ($\mathcal{K} > 0$).

3.1.3 RM *distributions*

Figs. 3(b) and 4(b) show the distribution for the RMs of the data sets, L_{DM} and L_{Ind}, respectively. The mean value for the RM subset of L_{DM} is measured at (23.59 ± 3.37) rad m^{-2}, with a large standard deviation of (124.01 ± 2.38) rad m^{-2}. In comparison, the L_{Ind} data set shows a higher mean of (36.37 ± 7.61) rad m^{-2} and large standard deviation of (117.91 ± 5.39) rad m^{-2}.

Both histograms indicate minimal $\mathcal{S}$ (more or less symmetric distribution) and $\mathcal{K} > 0$, suggesting heavy tails relative to a normal distribution. These characteristics imply that the data exhibit non-normal distribution traits. This is particularly noteworthy for RM, as the observed deviations suggest that the simple random walk model (see section 3.2 in A. Seta & C. Federrath 2021b) may not adequately capture the complexities of the Milky Way's magnetic field and the ISM. Instead, a more nuanced approach that considers factors such as magnetic field inhomogeneities and non-uniform electron density may be necessary for accurately describing the RM distribution. The non-normal characteristics observed likely stem from several underlying physical factors, which are discussed in Section 4.2.

3.1.4 DM *distributions*

Figs. 3(c) and 4(c) present histograms for the DMs of the data sets L_{DM} and L_{Ind}, respectively. The mean value for the DM subset of L_{DM} is measured at (195.29 ± 3.18) pc cm^{-3}, accompanied by a very large standard deviation of (173.92 ± 2.25) pc cm^{-3}. In contrast, the L_{Ind} data set shows a smaller mean of (114.76 ± 5.28) pc cm^{-3}, with a correspondingly smaller standard deviation of (102.29 ± 3.74) pc cm^{-3}.

Upon examining the distributions, we observe a significant right skewness, indicating a tendency for higher values. Moreover, the $\mathcal{K}$ values for both data sets are observed to be > 0, suggesting non-normal distributions. This non-normality is expected, as DM along the line of sight will be influenced by various astrophysical factors, such as variations in electron density due to different structures such as bubbles, filaments, and other features that can influence the dispersion measure, causing deviations from a normal distribution

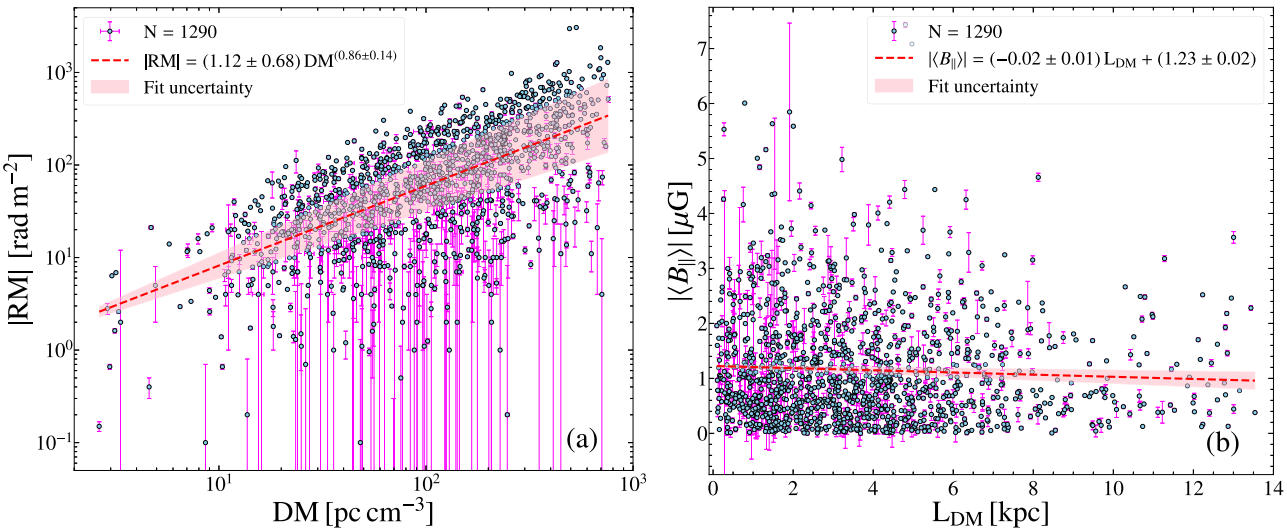

Figure 5. (a) A log–log plot of |RM| versus DM for the L_{DM} data set, with a linear fit in the log–log space shown as the red dashed line and the one-sigma deviations are shown as a pink band around it. The best-fitting line is given by $|RM| = (1.12 \pm 0.68)\,DM^{(0.86\pm0.14)}$. (b) A plot of the absolute value of the average parallel magnetic field $|\langle B_\parallel \rangle|$ versus distance, calculated using (4). The best-fitting line is shown as the red dashed line with one-sigma deviations as a pink band around it. The best-fitting line is given by $|\langle B_\parallel \rangle| = (-0.02 \pm 0.01)\,L_{DM} + (1.23 \pm 0.02)$. From these results, we conclude that $|RM| \propto DM$ and $|\langle B_\parallel \rangle| \propto L^0_{DM}$. From (b), on an average, $|\langle B_\parallel \rangle|| \approx 1.2$ μG (intercept of the fitted line).

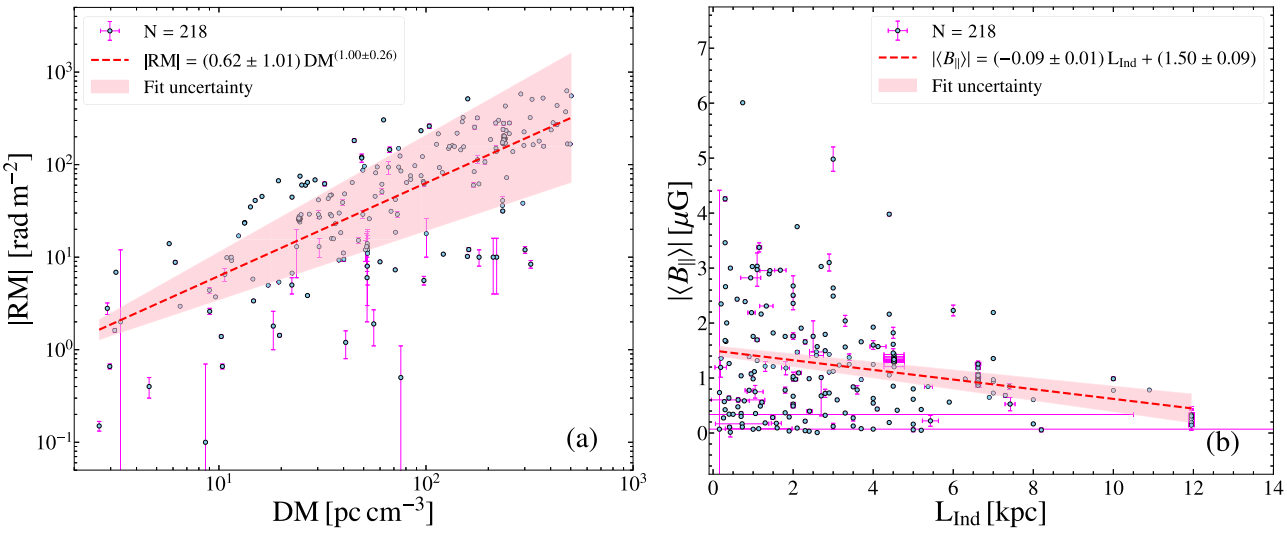

Figure 6. Same as Fig. 5 but for the L_{Ind} data set. Here, $|RM| = (0.62 \pm 1.01)\,DM^{(1.00\pm0.26)}$ and $|\langle B_\parallel \rangle| = (-0.09 \pm 0.01)\,L_{Ind} + (1.50 \pm 0.09)$. The conclusion that $|RM| \propto DM$ and $|\langle B_\parallel \rangle|$ are independent of the distance to the pulsar also roughly remains the same (although the level of uncertainties is higher given the smaller size of the data). For this data set, on average, $|\langle B_\parallel \rangle| \approx 1.5$ μG.

along the line of sight (A. A. Ruzmaikin et al. 1988; J. M. Cordes & T. J. W. Lazio 2002).

3.2 Parameter relationships: |RM| versus DM and $\langle B_\parallel \rangle$ versus distance

Figs. 5(a) and 6(a) present scatter plots (blue points) showing the absolute value of RMs and DMs for pulsars, including their associated uncertainties. Notably, the data set comprises 1290 pulsars for L_{DM} and 218 for L_{Ind}. The best-fitting line for the L_{DM} data set is given by $|RM| = (1.12 \pm 0.68)\,DM^{(0.86\pm0.14)}$, while for the L_{Ind} data set, it is $|RM| = (0.62 \pm 1.01)\,DM^{(1.01\pm0.26)}$. Both fits are consistent with a nearly linear scaling, $|RM| \propto DM$, which reflects the fact that the DM-dependence of RM is primarily set by fluctuations in the thermal electron density along the line of sight. If variations in the magnetic field dominated, we would expect a weaker or more scattered correlation.

Next, we examine the relationship between the distance to the pulsar and the estimated average magnetic field strength ($|\langle B_\parallel \rangle| = 1.232\ |RM|/DM$) in Fig. 5(b) for L_{DM} and Fig. 6(b) for L_{Ind}. The best-fitting line for the L_{DM} data set is given by $|\langle B_\parallel \rangle| = (-0.02 \pm 0.01)\,L_{Ind} + (1.23 \pm 0.02)$, while for the L_{Ind} data set, it is $|\langle B_\parallel \rangle| = (-0.09 \pm 0.01)\,L_{Ind} + (1.50 \pm 0.09)$. In both cases, the intercepts (1.2 and 1.5 μG) represent the average magnetic field strength, suggesting potentially an intrinsic baseline contribution from the large-scale Galactic field. Both slopes are close to zero,

Table 1. Summary of results for various data sets categorized by the distance condition, including $L_{DM} \leq 1$ kpc, $L_{DM} \leq 2$ kpc, $L_{DM} \leq 5$ kpc, $L_{DM} \leq 20$ kpc, and L_{Ind}. Each distance condition is analysed using three correlation functions, $\mathcal{C}_1$, $\mathcal{C}_2$, and $\mathcal{C}_3$. The table presents the number of data points (N) and the derived parameters, including c_0, Gl_0, Gb_0, and ℓ_b, along with their associated uncertainties. The parameters c_0, Gl_0, Gb_0, and ℓ_b exhibit slight variations with distance, particularly a decrease in c_0 with increasing distance (up to 5 kpc) and an increase in ℓ_b over the same range is observed. The results for the L_{Ind} data set are significantly different from others (except for the $L_{DM} \leq 1$ kpc case, where they are more similar). Additionally, within uncertainities, $\mathcal{C}_1$, $\mathcal{C}_2$, and $\mathcal{C}_3$ give similar ℓ_b values across distances.

Data set	N	$C(s)$	c_0(cm^{-3} μG)	Gl_0(°)	Gb_0(°)	ℓ_b(pc)
$L_{DM} \leq 1$ kpc	165	$\mathcal{C}_1$	0.06 ± 0.03	124 ± 29	51 ± 19	11 ± 5
$L_{DM} \leq 1$ kpc	165	$\mathcal{C}_2$	0.06 ± 0.03	124 ± 29	50 ± 19	14 ± 5
$L_{DM} \leq 1$ kpc	165	$\mathcal{C}_3$	0.06 ± 0.03	125 ± 31	54 ± 19	12 ± 5
$L_{DM} \leq 2$ kpc	397	$\mathcal{C}_1$	0.04 ± 0.01	119 ± 27	65 ± 12	35 ± 14
$L_{DM} \leq 2$ kpc	397	$\mathcal{C}_2$	0.04 ± 0.01	119 ± 26	65 ± 12	44 ± 14
$L_{DM} \leq 2$ kpc	397	$\mathcal{C}_3$	0.04 ± 0.01	111 ± 28	66 ± 13	40 ± 14
$L_{DM} \leq 5$ kpc	936	$\mathcal{C}_1$	0.05 ± 0.01	122 ± 10	66 ± 10	47 ± 17
$L_{DM} \leq 5$ kpc	936	$\mathcal{C}_2$	0.05 ± 0.01	123 ± 10	65 ± 10	57 ± 17
$L_{DM} \leq 5$ kpc	936	$\mathcal{C}_3$	0.04 ± 0.01	125 ± 11	65 ± 11	51 ± 17
$L_{DM} \leq 20$ kpc	1290	$\mathcal{C}_1$	0.05 ± 0.02	192 ± 9	36 ± 33	18 ± 8
$L_{DM} \leq 20$ kpc	1290	$\mathcal{C}_2$	0.05 ± 0.02	192 ± 9	36 ± 33	22 ± 8
$L_{DM} \leq 20$ kpc	1290	$\mathcal{C}_3$	0.05 ± 0.02	192 ± 9	36 ± 34	18 ± 8
L_{Ind}	218	$\mathcal{C}_1$	0.07 ± 0.02	133 ± 9	18 ± 30	4 ± 1
L_{Ind}	218	$\mathcal{C}_2$	0.07 ± 0.02	134 ± 9	18 ± 31	5 ± 1
L_{Ind}	218	$\mathcal{C}_3$	0.07 ± 0.02	134 ± 9	18 ± 30	4 ± 1

indicating no significant connection between $|\langle B_\parallel \rangle|$ and distance, suggesting that the average magnetic field strength remains consistent across the sampled pulsars, independent of the distance. However, the observed lack of significant correlation between $\langle B_\parallel \rangle$ and distance should not be taken as evidence of a uniformly strong magnetic field across all distances. Rather, this result likely stems from the averaging effect of integrating over large path lengths, which tends to smooth out smaller scale variations in the magnetic field.

However, this somewhat 'synthetic' uniformity over large kpc distances points to the importance of focusing on small-scale, localized variations within the magneto-ionic medium, where small-scale fluctuations become more prominent. These small-scale structures can often be masked by the large-scale averaging, but they play a very important role in shaping the overall behaviour of the magneto-ionic medium. This highlights the core methodology and aim of our work, to examine both the properties of the large-scale field and small-scale structures within the magneto-ionic medium together. By determining the correlation lengths, ℓ_b and $\ell_{\delta n_e}$, we can better understand the scale and impact of these small-scale variations, which are often masked in other analyses in the literature.

3.3 Table of results: $L_{DM} \leq 20$ kpc

The $L_{DM} \leq 20$ kpc data set contains the largest number of pulsars and serves as the reference point for our analysis. One of the most significant findings is the difference in the correlation lengths, ℓ_b and $\ell_{\delta n_e}$, across the different correlation functions.

The magnetic field correlation length, ℓ_b, ranges from (18 ± 8) pc for $\mathcal{C}_1$ and $\mathcal{C}_3$ to (22 ± 8) pc for $\mathcal{C}_2$. This indicates that small-scale magnetic fields are correlated over significantly short distances compared to the distance to the pulsar.

In contrast, the thermal electron density correlation length, $\ell_{\delta n_e}$, is significantly larger. For $\mathcal{C}_1$, $\ell_{\delta n_e}$ is (251 ± 12) pc, with $\mathcal{C}_2$ extending to (305 ± 12) pc, and $\mathcal{C}_3$ yielding (291 ± 12) pc. This difference, where ℓ_b ranges from 18 to 22 pc while $\ell_{\delta n_e}$ spans 251 to 305 pc, reveals that small-scale thermal electron density structures are much more extended, compared to the small-scale magnetic field structures.

The results show a fundamental difference in the scales at which magnetic fields and electron densities shape the magneto-ionic medium and the related radio observables. Magnetic fields have a more localized influence, while thermal electron density fluctuations extend across much larger scales. Recognizing and distinguishing these distinct scales is crucial for accurately interpreting RM from extragalactic sources and the dynamics of the magneto-ionic medium.

Moving to other parameters, the value of c_0 remains consistent across all three correlation functions ($\mathcal{C}_1$, $\mathcal{C}_2$, and $\mathcal{C}_3$), averaging around (0.05 ± 0.02) cm^{-3} μG, as shown in Table 1. The galactic coordinates Gl_0 and Gb_0, which serve as reference points for the large-scale magnetic field models, stabilize around $(192 \pm 9)^\circ$ for Gl_0 and $(36 \pm 33)^\circ$ for Gb_0, indicating that the large-scale magnetic field reference point is consistent across the correlation functions.

The average electron density, $\langle n_e \rangle$, also remains very stable across all correlation functions for $L_{DM} \leq 20$ kpc, with values consistently around (0.055 ± 0.001) cm^{-3}, as shown in Table 2. This agrees with values in the literature (B. M. Gaensler et al. 2008; J. M. Yao et al. 2017). The small error bars represent formal statistical uncertainties and do not include systematic effects from model assumptions, though the similar estimate with different distances may still imply a converged solution for the magnitude of the large-scale thermal electron density.

The calculated large-scale magnetic field strength, $|B|$, for $L_{DM} \leq 20$ kpc remains consistent across all correlation functions, with a value of approximately 1.2 ± 0.5 μG for $\mathcal{C}_1$, $\mathcal{C}_2$, and $\mathcal{C}_3$. It should be noted that B has large error bars, which is largely due to uncertainties in the parameter c_0, which stems from the relatively high uncertainty in RM observations compared to DM.

The main results obtained from our study are given in Tables 1, 2, and 3. Here, we discuss the interesting trends and important points from those results.

3.4 Accounting for non-Gaussianity in RM and DM distributions

Figs. 3 and 4 show that both the RM and DM distributions are non-Gaussian, with kurtosis ($\mathcal{K}$) significantly greater than zero. To assess the sensitivity of our results to this non-Gaussianity,

Table 2. The results and errors for $\langle n_e \rangle$ and $\ell_{\delta n_e}$, categorized by the distance conditions: $L_{DM} \leq 1$ kpc, $L_{DM} \leq 2$ kpc, $L_{DM} \leq 5$ kpc, $L_{DM} \leq 20$ kpc, and L_{Ind}. Similar to Table 1, the parameter $\langle n_e \rangle$ remains consistent across correlation functions, while $\ell_{\delta n_e}$ shows greater variation. Notably, $\langle n_e \rangle$ increases with distance up to 5 kpc. As in Table 1, the results for the L_{Ind} data set are significantly different except for the $L_{DM} \leq 1$ kpc case.

Data set	N	$C(s)$	$\langle n_e \rangle$ (cm^{-3})	$\ell_{\delta n_e}$(pc)
$L_{DM} \leq 1$ kpc	268	$\mathcal{C}_1$	0.106 ± 0.004	31 ± 10
$L_{DM} \leq 1$ kpc	268	$\mathcal{C}_2$	0.106 ± 0.004	37 ± 10
$L_{DM} \leq 1$ kpc	268	$\mathcal{C}_3$	0.104 ± 0.004	34 ± 10
$L_{DM} \leq 2$ kpc	693	$\mathcal{C}_1$	0.069 ± 0.002	89 ± 10
$L_{DM} \leq 2$ kpc	693	$\mathcal{C}_2$	0.069 ± 0.002	114 ± 10
$L_{DM} \leq 2$ kpc	693	$\mathcal{C}_3$	0.063 ± 0.002	115 ± 10
$L_{DM} \leq 5$ kpc	1898	$\mathcal{C}_1$	0.060 ± 0.001	178 ± 4
$L_{DM} \leq 5$ kpc	1898	$\mathcal{C}_2$	0.060 ± 0.001	250 ± 4
$L_{DM} \leq 5$ kpc	1898	$\mathcal{C}_3$	0.057 ± 0.001	252 ± 4
$L_{DM} \leq 20$ kpc	3077	$\mathcal{C}_1$	0.055 ± 0.001	251 ± 12
$L_{DM} \leq 20$ kpc	3077	$\mathcal{C}_2$	0.054 ± 0.001	305 ± 12
$L_{DM} \leq 20$ kpc	3077	$\mathcal{C}_3$	0.053 ± 0.001	291 ± 12
L_{Ind}	375	$\mathcal{C}_1$	0.033 ± 0.002	35 ± 15
L_{Ind}	375	$\mathcal{C}_2$	0.033 ± 0.002	60 ± 15
L_{Ind}	375	$\mathcal{C}_3$	0.033 ± 0.002	39 ± 15

Table 3. Large-scale magnetic field strength, $|B|$, along with their determined uncertainties for distance conditions: $L_{DM} \leq 1$ kpc, $L_{DM} \leq 2$ kpc, $L_{DM} \leq 5$ kpc, $L_{DM} \leq 20$ kpc, and L_{Ind}, and are further divided into three correlation functions, $\mathcal{C}_1$, $\mathcal{C}_2$, and $\mathcal{C}_3$. The form of the correlation function does not play a major role in the derived large-scale magnetic field strengths. Notably, $|B|$ tends to increase slightly with distance, and the values for the L_{Ind} data set are higher than those for L_{DM}. This discrepancy suggests a potential bias in the sample with independently determined pulsar distances.

Data set	$C(s)$	$\lvert B \rvert$(μG)
$L_{DM} \leq 1$ kpc	C_1	0.7 ± 0.3
$L_{DM} \leq 1$ kpc	C_2	0.7 ± 0.3
$L_{DM} \leq 1$ kpc	C_3	0.7 ± 0.3
$L_{DM} \leq 2$ kpc	C_1	0.8 ± 0.3
$L_{DM} \leq 2$ kpc	C_2	0.8 ± 0.3
$L_{DM} \leq 2$ kpc	C_3	0.8 ± 0.3
$L_{DM} \leq 5$ kpc	C_1	0.9 ± 0.3
$L_{DM} \leq 5$ kpc	C_2	0.9 ± 0.3
$L_{DM} \leq 5$ kpc	C_3	0.9 ± 0.3
$L_{DM} \leq 20$ kpc	C_1	1.2 ± 0.5
$L_{DM} \leq 20$ kpc	C_2	1.2 ± 0.5
$L_{DM} \leq 20$ kpc	C_3	1.2 ± 0.5
L_{Ind}	C_1	2.7 ± 0.6
L_{Ind}	C_2	2.5 ± 0.6
L_{Ind}	C_3	2.6 ± 0.6

we draw ϵ_{RM} in equation (22) and η_{DM} in equation (38) from random, non-Gaussian distributions (also, always making sure that DM > 0 pc cm^{-3}). These non-Gaussian distributions are generated using the Fleishman transformation (A. I. Fleishman 1978), which allows us to set the skewness and kurtosis while preserving the empirical mean and standard deviation of the data. For both RM and DM, we set the skewness to zero, consistent with the near-symmetric observed distributions, and tested our method across a range of kurtosis values ($\kappa = 0, 0.1, 1, 2, 5$). For each κ, we repeated the full parameter estimation procedure outlined in Sections 2.1–2.4.

We find that the fitted parameters, in particular c_0, ℓ_b, and $\ell_{\delta n_e}$, remain consistent with those obtained under the Gaussian assumption, within their respective uncertainties. This demonstrates that our results are robust to deviations from Gaussianity in the RM and DM distributions. The results for the non-Gaussian distributions are presented and further discussed in Appendix C.

3.5 Impact of distance on c_0, Gl_0, Gb_0, and ℓ_b

Originally, we wanted to study how different parts of the Milky Way influence the properties of the magnetic field and thermal electron density, especially ℓ_b and $\ell_{\delta n_e}$. Focusing our attention mainly on the Galactic disc, where most of the gas and star-forming activity is expected, we tried to isolate these effects by limiting the data set only to Gb values between -5° and $+5^\circ$. However, with a limited number of pulsars (N = 120) in this range, we were unable to obtain statistically robust fits.

We also attempted to separate the pulsar sample into longitude-based subsamples: one roughly aligned with the local spiral arms ($85^\circ \leq Gl \leq 95^\circ$ and $265^\circ \leq Gl \leq 275^\circ$), which should predominantly probe the local large-scale magnetic field and one in the perpendicular direction ($355^\circ \leq Gl \leq 5^\circ$ and $175^\circ \leq Gl \leq 185^\circ$), which should be more sensitive to the random component of the magnetic field. Unfortunately, the available number of pulsars in these restricted regions ($N = 49$ and $N = 115$, respectively) was too small to obtain statistically converged results.

We therefore focused in this paper on the broader distance-limited samples (1, 2, 5, and 20 kpc), which provide statistically stable and converged estimates of the magnetic field and electron density parameters. None the less, the subsample analysis highlights the limitations of current data sets in probing localized magnetic field structures. Future surveys, particularly with SKA (E. Keane et al. 2015), are expected to provide much larger and more uniformly distributed pulsar samples, at which point such region-specific analyses will become feasible and yield more localized constraints on the Galactic magnetic field.

The results in Table 1 reveal an interesting trend in the magnetic field parameters as a function of the cutoff distance to the pulsars. The correlation length ℓ_b shows variation with distance, suggesting the influence of different ISM regions on the correlation length. For $L_{DM} \leq 2$ kpc, ℓ_b values increase, reaching (35 ± 14) pc for $\mathcal{C}_1$, (44 ± 14) pc for $\mathcal{C}_2$, and (40 ± 14) pc for $\mathcal{C}_3$. As the distance extends to $L_{DM} \leq 5$ kpc, ℓ_b values continue to increase, with ℓ_b reaching (47 ± 17) pc for $\mathcal{C}_1$, $(57 \pm 167$ pc for $\mathcal{C}_2$, and (51 ± 17) pc for $\mathcal{C}_3$. These larger ℓ_b values may indicate regions where the magnetic field is more coherent and less random, suggesting that the ISM's large-scale structure becomes more prominent as the sightline extends through different ISM environments, including more quiescent regions or spiral arms. A caveat could also be that with a decreasing number of pulsars in the data set with smaller distances (N), the separation between the small- and large-scale might not be as good, potentially contaminating the estimated ℓ_b. Furthermore, the significant differences in some parameters for $L_{DM} \leq 5$ kpc and $L_{DM} \leq 20$ kpc may be due to contributions from the known large-scale magnetic field reversal, which affects the RMs of distant pulsars. In addition, some of these pulsars probe distant regions within the same spiral arm, where the line-of-sight magnetic field could be opposite to that in the nearby part of the arm.

We note that although some inferred values of Gb_0 in Table 1 appear large, their uncertainties are substantial, particularly for larger distance cuts (e.g. $L_{DM} \leq 20$, kpc). Within these uncertainties, the results remain consistent with Gb_0 close to 0°, in agreement with the established view that the Galactic magnetic field lies largely parallel to the plane (J. L. Han 2017). At smaller distances, the scatter in Gb_0 reflects the reduced number of pulsars and limited line-of-

sight coverage, and we therefore interpret the apparent variations as sampling effects rather than evidence of a significant vertical field.

The inferred Gl_0 values also differ somewhat from earlier pulsar- and extragalactic source-based studies. These shifts primarily occur because our analysis simultaneously models both large- and small-scale components using a larger pulsar data set, which can alter the best-fitting orientation. None the less, our results are broadly consistent within uncertainties, complementing earlier estimates and highlighting the influence of different data sets and modelling approaches.

3.6 Impact of distance on $\langle n_e \rangle$, $\ell_{\delta n_e}$, and $|B|$

The correlation length $\ell_{\delta n_e}$ shows significant variability with distance. At shorter distances ($L_{DM} \leq 1$ kpc), $\ell_{\delta n_e}$ values range from 31 to 37 pc, indicating the influence of smaller scale structures. However, as the distance extends to $L_{DM} \leq 5$ kpc, $\ell_{\delta n_e}$ increases dramatically to over ~ 250 pc, suggesting that the magneto-ionic structures become more correlated over larger spatial scales at greater distances.

In contrast, the average electron density $\langle n_e \rangle$, remains relatively stable across different distances. At shorter distances ($L_{DM} \leq 1$ kpc), $\langle n_e \rangle$ is around $0.106 \pm 0.004\,cm^{-3}$, gradually decreasing to $0.060 \pm 0.001\,cm^{-3}$ by $L_{DM} \leq 5$ kpc. This steady decline reflects the more diffuse nature of the magneto-ionic medium at greater distances.

Magnetic field strength, $|B|$, derived from c_0 and $\langle n_e \rangle$, remains consistent across the sampled distances, averaging around $1.2 \pm 0.5\,\mu G$ up to $L_{DM} \leq 20$ kpc. Although, for all cases, the uncertainties are significant ($\approx$ 30–40 per cent) but this remains true across all the sampled distances for the L_{DM} data set. The value of $\approx 1\,\mu G$ is broadly consistent with that inferred from polarized synchrotron emission observations (R. Beck 2016).

3.7 Data set variations: L_{DM} versus L_{Ind}

The L_{Ind} data set, which utilizes independently obtained pulsar distances (distance estimated without taking into account the pulsar DMs), shows significant differences compared to the L_{DM} data set. In particular, the magnetic correlation length, ℓ_b, is significantly smaller (4–5 pc), indicating that really local fluctuations dominate this data set, possibly due to selection biases such as 'clustered' pulsars in globular clusters (see bunches at the same distances in Fig. 6b).

Both $\langle n_e \rangle$ and $\ell_{\delta n_e}$ are lower in the L_{Ind} data set compared to L_{DM}. $\langle n_e \rangle$ hovers around $(0.033 \pm 0.002)\,cm^{-3}$, while $\ell_{\delta n_e}$ ranges from 35 to 60 pc, reflecting the more localized structures sampled in L_{Ind}. These lower values suggest that this data set captures different aspects of the magneto-ionic medium, likely more influenced by the local ISM environments.

The $|B|$ values in the L_{Ind} data set are also higher, ranging from (2.5 ± 0.6) to $(2.7 \pm 0.6)\,\mu G$. These larger values may result from the smaller ℓ_b and $\ell_{\delta n_e}$ in these environments, which lead to stronger magnetic field estimates when averaging over shorter distances. However, it's important to note that the error bars are larger in the L_{Ind} data set due to its significantly smaller sample size. This further underscores the influence of environmental factors and potential selection biases, which are further explored in Section 4.3.

4 DISCUSSION

4.1 Difference between ℓ_b and $\ell_{\delta n_e}$

The stark contrast between ℓ_b and $\ell_{\delta n_e}$ highlights that different physical processes within the Milky Way's magneto-ionic medium control their properties. While RM traces the product of thermal electron density and line-of-sight magnetic field strength, DM reflects the total electron column density (e.g. see section 2 of S. Hutschenreuter et al. 2024). Our results show that ℓ_b is much smaller (around 20–30 pc) compared to $\ell_{\delta n_e}$, which spans 250–300 pc. This indicates that magnetic field fluctuations occur on much shorter spatial scales, whereas electron density variations persist over much larger scales. This also suggests that magnetic fields and electron densities probably respond to different dominant physical mechanisms.

Regions of high turbulence, such as those affected by star formation, supernovae, or spiral arm shocks, experience intense dynamical processes. These events disrupt magnetic field lines, leading to tangling and compression that reduce magnetic coherence, reflected in smaller ℓ_b values (A. Seta et al. 2020; K. Ferrière 2020; A. Ricarte, R. Qiu & R. Narayan 2021; A. Seta & C. Federrath 2021a). In contrast, beyond turbulence, small-scale electron density structures are likely shaped by one or more large-scale H II regions (sizes in the range 10–200 pc, see M. Azimlu et al. 2011), which ionize the surrounding medium, probably explaining the larger $\ell_{\delta n_e}$.

Small-scale magnetic fields in the ISM are expected to be strongly influenced by turbulence and dynamo action (F. Rincon 2019). Numerical simulations at modest values of the magnetic Reynolds number (Rm of the order of 10^3) produce magnetic correlation scales that are a fraction (1/2–1/3) of the turbulence driving scale (e.g. A. A. Schekochihin et al. 2004; N. E. Haugen et al. 2004; P. Bhat & K. Subramanian 2013; S. Sur, P. Bhat & K. Subramanian 2018; A. Seta et al. 2020; A. Seta & C. Federrath 2021a). Given the realistic ISM conditions, however, Rm is expected to be much larger ($\approx 10^{18}$, see table 1 in A. Brandenburg & K. Subramanian 2005). The final state of the dynamo-generated magnetic fields at such high Rms remains unsettled but analytical models suggest that the field properties approach those at the critical value of Rm for the dynamo action ($\approx 10^2$, see table III in A. Seta et al. 2020) due to strong non-linearity (K. Subramanian 1999, 2003). Assuming this is the case and the turbulence is driven by supernova explosions at $\ell_{driv} \approx 100$ pc, the estimated values of ℓ_b (20–30 pc) are consistent with the turbulent dynamo action at smaller scales. We also note that some dynamo theories predict a final magnetic correlation scale as $\approx \ell_{driv}\,Rm^{-1/2}$ (see P. K. Dittrikh et al. 1988) and this would yield an unrealistically small magnetic field correlation scale.

This distinction between ℓ_b and $\ell_{\delta n_e}$ is crucial for interpreting RM data, particularly from extragalactic sources where DM is often unavailable (except for FRBs). While extragalactic RMs provide broad sky coverage, they lack the n_e information that pulsar DMs offer, complicating the separation of magnetic and electron density contributions (N. Oppermann et al. 2012; S. Hutschenreuter & T. A. Enßlin 2020; S. Hutschenreuter et al. 2022, 2024; C. L. Van Eck et al. 2023). Future FRB data sets, which directly provide DMs, will help bridge this gap and improve the joint use of RM and DM to probe both the Galactic and extragalactic magneto-ionic media (D. R. Lorimer et al. 2007; V. Ravi et al. 2016).

4.2 Non-Gaussian RM distribution

The non-normal distribution of RM, shown in Figs. 3(b) and 4(b), likely arises from multiple factors:

(i) Magnetic field structure: The Milky Way's magnetic field includes both large-scale, regular fields, such as those in spiral arms (R. Beck et al. 2019; Y. K. Ma et al. 2020), and small-scale random fields. A simple combination of a large-scale field with Gaussian

random fluctuations would result in a shifted Gaussian distribution, i.e. a Gaussian with a non-zero mean. But this combination at different levels for different regions within the Milky Way, especially with arm and interarm contrast (A. Shukurov 1998), might introduce non-Gaussianity.

(ii) Non-uniform electron density: The ionized gas in the Milky Way varies due to localized ionization sources and the multiphase ISM (T. Ha et al. 2023). Variations from H II regions, supernova remnants (SNRs), and enhanced star formation can add complexity to the RM distribution.

(iii) Magnetic field–thermal electron density correlation: Throughout our method, we assume that the magnetic field and thermal electron density are uncorrelated. However, on much smaller sub-kpc scales, such a correlation could probably exist due to shock compression. This makes the RM distribution significantly non-Gaussian (this is observed in RM distributions derived from turbulent magnetohydrodynamic simulations, e.g. see fig. 3(a) in A. Seta & C. Federrath 2021b).

(iv) ISM inhomogeneities: The inhomogeneous ISM, with structures like filaments, bubbles, and voids, further complicates the RM distribution (D. Martizzi, C.-A. Faucher-Giguère & E. Quataert 2015).

(v) Sample inhomogeneities: The pulsar sample is far from uniform (see Fig. 2) and thus such a non-uniform sampling might introduce significant deviations from Gaussianity.

Finding the exact reason for the observed non-Gaussianity in RM distributions requires further work and a combination of observational data, numerical simulations, and analytical models (especially with regards to other relevant observations, in particular H I and Hα observations, see F. Boulanger et al. 2018).

4.3 Considering pulsars as probes of the Galactic magnetic fields

Pulsars provide a valuable tool for probing the Milky Way's magnetic field, though their use comes with certain limitations due to environmental factors, line-of-sight averaging, uneven spatial distribution, and uncertainties in distance estimates. Often located in turbulent environments like SNRs and star-forming regions, pulsars are associated with high-density ionized gas and enhanced local magnetic fields, which can skew RM and DM measurements, making them less representative of the broader magneto-ionic medium (K. Ferrière 2001; B. M. Gaensler et al. 2008; M. Haverkorn et al. 2008).

Additionally, pulsars are clustered around the Galactic Centre, spiral arms, and globular clusters, where star formation is active and magnetic fields are stronger, resulting in a geographic bias toward higher RM and DM values (R. N. Manchester et al. 2005). This uneven distribution may lead to overestimations in parameters like $\langle n_e \rangle$ and $|B|$, while quieter, less active regions are undersampled, complicating generalizations about the Galactic magnetic field.

Additionally, scattering effects in dense ISM regions broaden pulsar signals, distorting RM and DM measurements (this distortion can also be used to study the intervening ISM properties, see C. Sobey et al. 2021; L. S. Oswald et al. 2021; W. C. Jing et al. 2025) and masking small-scale magnetic variations through line-of-sight averaging. Together, these effects smooth out local fluctuations, presenting a more uniform but potentially misleading picture of the magnetic field.

Pulsar distances are often estimated using electron density models (J. M. Cordes & T. J. W. Lazio 2002; J. M. Yao et al. 2017), which can have considerable uncertainties, especially in complex regions (e.g. see K. I. I. Koljonen et al. 2024). The independent distance in L_{Ind} data set does address this issue partially, but the current small data size, combined with probable biases, makes it difficult to fully utilize their potential and also compare the results with the L_{DM} data set.

4.4 Assumptions and related caveats

Throughout our analysis, driven by the analytical nature of the work and the limitations of the available data, we have made some simplifying assumptions. Here, we discuss the possible implications of the major assumptions in the study and the related caveats.

Our large-scale magnetic field model, equation (10), assumes that the field is unidirectional and does not capture the complexities of the Galactic magnetic fields, especially the details of the spiral structure and the presence of large-scale magnetic field reversals. Several models in the literature include details of the large-scale magnetic field structure (X. H. Sun et al. 2008; C. L. Van Eck et al. 2011; R. Jansson & G. R. Farrar 2012; A. Shukurov et al. 2019). Unlike our simplistic model, such models have a large number of empirical or physical parameters for which the current data are severely limited (Fig. 2) and these models also do not agree with each other (e.g. see fig. 8 in Y. K. Ma et al. 2020). Thus, some of the RM fluctuations that we associate with the small-scale magnetic field (e.g. in equation 14) might stem from significant spatial variations in the large-scale magnetic fields.

For modelling small-scale components, we study three well-motivated correlation functions (Section 2.3) but such two-point statistics do not account for the non-Gaussian structure of the magnetic fields. It is well known from theory (e.g. Ya. B. Zeldovich, A. A. Ruzmaikin & D. D. Sokoloff 1990; K. Subramanian 1998) and simulations (e.g. A. Seta et al. 2020; A. Seta & C. Federrath 2022) that the small-scale random magnetic fields are spatially intermittent or highly non-Gaussian. The effect of such random, non-Gaussian structures on RM statistics is relatively unknown. However, for large kpc distances to pulsars (where the ratio of the random magnetic field scale to the typical pulsar distance is significantly less than one), the small-scale structure might not matter much for the RM distribution due to the central limit theorem (assuming point-to-point uncorrelated thermal electron density and magnetic fields).

As discussed in Section 2.1, we assume that the large- and small-scale fields are independent of each other but the tangling of the large-scale field by turbulence could introduce small-scale, random magnetic fluctuations (see appendix A in A. Seta et al. 2018, for a brief discussion). Thus, they are strictly not independent of each other. Considering such non-trivial connections analytically requires further work but that might introduce corrections to the derived results.

Finally, the pulsar sample is not large enough to differentiate based on specific objects, such as known H II or dense regions, along the line of sight (e.g. as shown in C. Sobey et al. 2021; S. K. Ocker et al. 2024). This might introduce inhomogeneities in the sample that are currently not accounted for by the model. So, some of the overall RM and DM variations might be due to these specific line-of-sight effects.

Overall, the currently available data and simplistic modelling allow us to work primarily analytically (except for the numerical minimization discussed in Section 2.4) to study some important parameters of the Galactic thermal electron density and magnetic fields, especially the correlation lengths of their small-scale components, and we aim to explore the impact of these assumptions in our future work.

5 CONCLUSIONS

The magneto-ionic medium of the Milky Way, i.e. the thermal electron density in the ionized gas and the magnetic fields, can be divided into large- and small-scale components. This study provides important insights into the structure and dynamics of the magneto-ionic medium of the Milky Way through a comprehensive analysis of pulsar data from the ATNF pulsar catalogue (R. N. Manchester et al. 2005, version 2.4.0). In particular, we determine the strength of the large-scale components of the thermal electron density and magnetic fields and scales of their respective small-scale components. Using the dispersion (DM) and rotation (RM) measures of pulsars and analytical models, we have obtained estimates of different properties of thermal electron density and magnetic fields. The main results of the work are given below.

(i) |RM|versusDM: The analysis showed a strong power-law relationship between the pulsar |RM| and DM (Figs. 5a and 6a). From this, we can conclude that |RM| $\propto$ DM, which further demonstrates the role of distance; the further away pulsars, accumulate higher DM and, by extension, |RM|.

(ii) *Average magnetic field strength versus distance:* We see a clear lack of correlation between the average parallel magnetic field strength, $\langle B_\parallel \rangle = 1.232\,\mathrm{RM/DM}$, with the distance to the pulsar (Figs. 5b and 6b). It indicates that, for RM, the large-scale magnetic field structure dominates over the sampled distances, with smaller scale fluctuations averaged out over the path length (further motivating a scale separation of the Galactic magnetic field). However, this does not necessarily imply a uniform large-scale field, and with our method (Section 2), we determine the large-scale field strength ($\sim 1.2\,\mu$G for distances $\leq 20\,$kpc, see Table 3 for further details) instead of the average magnetic field strength along the line of sight.

(iii) *Correlation length of small-scale components:* Most importantly, we estimate the scale of the small-scale magnetic field and thermal electron density (see Tables 1 and 2). The difference between the correlation length of the magnetic field (ℓ_b) and the correlation length of the thermal electron density ($\ell_{\delta n_e}$) is one of the most striking outcomes of this study. We found that ℓ_b is much smaller, within 20–30 pc, compared to $\ell_{\delta n_e}$, which is in the range of 250–300 pc. Physically, ℓ_b can be seen to be consistent with the theoretical expectations from the turbulent dynamo simulations and $\ell_{\delta n_e}$ with the scales of one or multiple large H II regions (see Section 4.1). When studying the magneto-ionic medium or interpreting the extragalactic RM observations, it is imperative to consider these results because of the very different scales of the thermal electron density and magnetic fields (a factor of ≈ 10).

(iv) *Impact of the assumed correlation function for the small-scale components:* The choice of correlation function ($\mathcal{C}_1$, $\mathcal{C}_2$, or $\mathcal{C}_3$, Fig. 1) has practically no effect on the estimated correlation lengths, ℓ_b and $\ell_{\delta n_e}$. Also, large-scale properties of the magneto-ionic medium, such as the mean thermal electron density ($\sim 0.05\,\mathrm{cm}^{-3}$) and the large-scale magnetic field strength ($\sim 1.2\,\mu$G), remain stable across all correlation functions and are consistent with previous studies.

In summary, this study sheds light on the complex structure of the Milky Way's magneto-ionic medium and demonstrates a mathematically concrete way to compute small-scale thermal electron density and magnetic field length scales that factor in the path length and the correlation structure of the random fields. These results can be considered as the starting point for further work that will help sharpen the information about the Galactic magnetic fields and their role in the dynamics and evolution of the Galaxy.

ACKNOWLEDGEMENTS

We thank our referee, Anvar Shukurov, for a careful review of this work and for providing insightful comments that helped improve the clarity and rigour of the manuscript. We thank Charlotte Sobey, Yik Ki Ma, Hiep Nguyen, and Naomi M. McClure-Griffiths for useful discussions. AS acknowledges support from the Australian Research Council's Discovery Early Career Researcher Award (DECRA, project DE250100003) and the Australia–Germany Joint Research Cooperation Scheme of Universities Australia (UA–DAAD, 2025–2026). This publication is adapted in part from the lead author's Honours thesis at the Australian National University.

DATA AVAILABILITY

The data used in the main text of the study are taken from the Australian National Telescope Facility (ATNF) pulsar catalogue (R. N. Manchester et al. 2005, version 2.4.0, https://www.atnf.csiro.au/research/pulsar/psrcat). In the appendix, the data from table IV.1 of A. A. Ruzmaikin et al. (1988) is used. No new data were generated in this research.

REFERENCES

Akahori T., Ryu D., Gaensler B. M., 2016, ApJ, 824, 105
Azimlu M., Barmby P., Marciniak R., 2011, American Astronomical Society Meeting Abstracts, Vol. 218, 106.02
Beck R., 2016, ARA&A, 24, 4
Beck R., Brandenburg A., Moss D., Shukurov A., Sokoloff D., 1996, ARA&A, 34, 155
Beck R., Shukurov A., Sokoloff D., Wielebinski R., 2003, A&A, 411, 99
Beck R., Chamandy L., Elson E., Blackman E. G., 2019, Galaxies, 8, 4
Bhat P., Subramanian K., 2013, MNRAS, 429, 2469
Boulanger F. et al., 2018, J. Cosmol. Astropart. Phys., 2018, 049
Brandenburg A., Subramanian K., 2005, Phys. Rep., 417, 1
Cordes J. M., Lazio T. J. W., 2002, preprint(astro-ph/0207156)
Deller A. T. et al., 2019, ApJ, 875, 100
Dittrikh P. K., Molchanov S. A., Ruzmaikin A. A., Sokolov D. D., 1988, Magnetohydrodynamics, 24, 274
Ferrière K., 2001, Rev. Mod. Phys., 73, 1031
Ferrière K., 2020, Plasma Phys. Control. Fusion, 62, 014014
Fleishman A. I., 1978, Psychometrika, 43, 521
Gaensler B. M., Madsen G. J., Chatterjee S., Mao S. A., 2008, PASA, 25, 184
Ha T., Li Y., Kounkel M., Xu S., Li H., Zheng Y., 2023, American Astronomical Society Meeting Abstracts, 228.01
Hackstein S., Brüggen M., Vazza F., Gaensler B. M., Heesen V., 2019, MNRAS, 488, 4220
Han J. L., 2017, ARA&A, 55, 111
Han J. L., Manchester R. N., Qiao G. J., 1999, MNRAS, 306, 371
Han J. L., Manchester R. N., Lyne A. G., Qiao G. J., van Straten W., 2006, ApJ, 642, 868
Han J. L., Manchester R. N., van Straten W., Demorest P., 2018, ApJS, 234, 11
Hartman J. W., Bhattacharya D., Wijers R., Verbunt F., 1997, A&A, 322, 477
Haugen N. E., Brandenburg A., Dobler W., 2004, Phys. Rev. E, 70, 016308
Haverkorn M., 2015, in Lazarian A., de Gouveia Dal Pino E. M., Melioli C., eds, Astrophysics and Space Science Library, Vol. 407, Magnetic Fields in Diffuse Media. Springer, Berlin, p. 483
Haverkorn M., Brown J. C., Gaensler B. M., McClure-Griffiths N. M., 2008, ApJ, 680, 362
Hewish A., Bell S. J., Pilkington J. D. H., Scott P. F., Collins R. A., 1968, Nature, 217, 709
Hollins J. F., Sarson G. R., Shukurov A., Fletcher A., Gent F. A., 2017, ApJ, 850, 4
Hutschenreuter S., Enßlin T. A., 2020, A&A, 633, A150
Hutschenreuter S. et al., 2022, A&A, 657, A43

Hutschenreuter S., Haverkorn M., Frank P., Raycheva N. C., Enßlin T. A., 2024, A&A, 690, A314
Indrani C., Deshpande A. A., 1999, New Astron., 4, 33
Jansson R., Farrar G. R., 2012, ApJ, 757, 14
Jing W. C. et al., 2025, preprint (arXiv:2506.14519)
Jokipii J. R., Lerche I., 1969, ApJ, 157, 1137
Jones D. I., Igoshev A. P., Haverkorn M., 2016, MNRAS, 460, 3298
Keane E. et al., 2015, in Advancing Astrophysics with the Square Kilometre Array (AASKA14). p. 40 preprint (arXiv:1501.00056)
Klein U., Fletcher A., 2015, Galactic and Intergalactic Magnetic Fields. Springer Praxis Books, Springer International Publishing, Heidelberg, Germany
Koljonen K. I. I., Lindseth S. S., Linares M., Harding A. K., Turchetta M., 2024, MNRAS, 529, 575
Krumholz M. R., Federrath C., 2019, Front. Astron. Space Sci., 6, 7
Lee C. P., Bhat N. D. R., Sokolowski M., Meyers B. W., Magro A., 2024, Publ. Astron. Soc. Aust., 41, e080
Lorimer D. R., Kramer M., 2012, Handbook of Pulsar Astronomy. Cambridge Univ. Press, Cambridge
Lorimer D. R., Bailes M., McLaughlin M. A., Narkevic D. J., Crawford F., 2007, Science, 318, 777
Lyne A. G., Smith F. G., 1989, MNRAS, 237, 533
Ma Y. K., Mao S. A., Ordog A., Brown J. C., 2020, MNRAS, 497, 3097
Manchester R. N., 1972, ApJ, 172, 43
Manchester R. N., 1974, ApJ, 188, 637
Manchester R. N., Hobbs G. B., Teoh A., Hobbs M., 2005, AJ, 129, 1993
Martin-Alvarez S. et al., 2024, ApJ, 966, 43
Martizzi D., Faucher-Giguère C.-A., Quataert E., 2015, MNRAS, 450, 504
Mitra D., Wielebinski R., Kramer M., Jessner A., 2003, A&A, 398, 993
Moran A., Mingarelli C. M. F., Bedell M., Good D., Spergel D. N., 2023, ApJ, 954, 89
Nelemans G., Hartman J. W., Verbunt F., Bhattacharya D., Wijers R. A. M. J., 1997, A&A, 322, 489
Newville M., Stensitzki T., Allen D. B., Ingargiola A., 2015, LMFIT: Non-Linear Least-Square Minimization and Curve-Fitting for Python. Available at: https://doi.org/10.5281/zenodo.11813
Ocker S. K., Anderson L. D., Lazio T. J. W., Cordes J. M., Ravi V., 2024, ApJ, 974, 10
Oppermann N. et al., 2012, A&A, 542, A93
Ordog A., Brown J. C., Kothes R., Landecker T. L., 2017, A&A, 603, A15
Oswald L. S. et al., 2021, MNRAS, 504, 1115
Pattle K., Fissel L., Tahani M., Liu T., Ntormousi E., 2023, in Inutsuka S., Aikawa Y., Muto T., Tomida K., Tamura M., eds, ASP Conf. Ser. Vol. 534, Protostars and Planets VII. Astron. Soc. Pac., San Francisco, p. 193
Planck Collaboration XIII 2016, A&A, 586, A138
Prochaska J. X. et al., 2019, Science, 366, 231
Rand R. J., Kulkarni S. R., 1989, ApJ, 343, 760
Ravi V. et al., 2016, Science, 354, 1249
Ricarte A., Qiu R., Narayan R., 2021, MNRAS, 505, 523
Rincon F., 2019, J. Plasma Phys., 85, 205850401
Ruszkowski M., Pfrommer C., 2023, A&AR, 31, 4
Ruzmaikin A. A., Sokoloff D. D., Shukurov A. M., eds., 1988, Magnetic fields of galaxies, Astrophysics and Space Science Library, Vol. 133. Springer, Dordrecht
Savage B. D., Wakker B. P., 2009, ApJ, 702, 1472
Schekochihin A. A., Cowley S. C., Taylor S. F., Maron J. L., McWilliams J. C., 2004, ApJ, 612, 276
Seta A., Federrath C., 2020, MNRAS, 499, 2076
Seta A., Federrath C., 2021a, Phys. Rev. Fluids, 6, 103701
Seta A., Federrath C., 2021b, MNRAS, 502, 2220
Seta A., Federrath C., 2022, MNRAS, 514, 957
Seta A., Federrath C., 2024, MNRAS, 533, 1875
Seta A., McClure-Griffiths N. M., 2025, MNRAS, 539, 1024
Seta A., Shukurov A., Wood T. S., Bushby P. J., Snodin A. P., 2018, MNRAS, 473, 4544
Seta A., Bushby P. J., Shukurov A., Wood T. S., 2020, Phys. Rev. Fluids, 5, 043702
Seta A., Federrath C., Livingston J. D., McClure-Griffiths N. M., 2023, MNRAS, 518, 919
Shetty R., Ostriker E. C., 2006, ApJ, 647, 997
Shukurov A., 1998, MNRAS, 299, L21
Shukurov A., Subramanian K., 2021, Astrophysical Magnetic Fields: From Galaxies to the Early Universe, Cambridge Astrophysics. Cambridge Univ. Press, Cambridge
Shukurov A., Snodin A. P., Seta A., Bushby P. J., Wood T. S., 2017, ApJ, 839, L16
Shukurov A., Rodrigues L. F. S., Bushby P. J., Hollins J., Rachen J. P., 2019, A&A, 623, A113
Smith F. G., 1968, Nature, 218, 325
Sobey C. et al., 2019, MNRAS, 484, 3646
Sobey C. et al., 2021, MNRAS, 504, 228
Subramanian K., 1998, MNRAS, 294, 718
Subramanian K., 1999, Phys. Rev. Lett., 83, 2957
Subramanian K., 2003, Phys. Rev. Lett., 90, 245003
Sun X. H., Reich W., Waelkens A., Enßlin T. A., 2008, A&A, 477, 573
Sur S., Bhat P., Subramanian K., 2018, MNRAS, 475, L72
Van Eck C. L. et al., 2011, ApJ, 728, 97
Van Eck C. L. et al., 2023, ApJS, 267, 28
Verbiest J. P. W., Weisberg J. M., Chael A. A., Lee K. J., Lorimer D. R., 2012, ApJ, 755, 39
Yao J. M., Manchester R. N., Wang N., 2017, ApJ, 835, 29
Zeldovich Y., Ruzmaikin A., Sokoloff D., Kleczek J., 1986, Astrophys. Space Sci., 120, 155
Zeldovich Ya. B., Ruzmaikin A. A., Sokoloff D. D., 1990, The Almighty Chance. World Scientific, Singapore

APPENDIX A: DERIVATION OF CORRELATION FUNCTIONS

In this work, we utilized three correlation functions to analyse the small-scale magnetic field and electron density fluctuations within the magneto-ionic medium. These three functions are defined and discussed in detail in Section 2.3. In this section, we outline the derivation to compute the contribution of each correlation function to the variance of small-scale fluctuations (see Sections 2.1 and 2.2 for the use of this variance).

A1 $\mathcal{C}_1$

For the exponential correlation function,

$$\mathcal{C}_1(s) = \mathcal{C}_0 \exp\left(-s/\ell\right), \tag{A1}$$

we want to solve

$$\sigma^2 = 2\int_0^L (L-s)\mathcal{C}_1(s)\,\mathrm{d}s. \tag{A2}$$

Substituting $\mathcal{C}_1$ and evaluating the integral (e.g. via integration by parts) gives

$$\sigma^2 = 2\mathcal{C}_0\left[\ell^2\exp(-L/\ell) - \ell^2 + L\ell\right]. \tag{A3}$$

This provides a compact expression for the variance in terms of $\mathcal{C}_0$, ℓ, and L.

A2 $\mathcal{C}_2$

For $\mathcal{C}_2$, we have

$$\mathcal{C}_2(s) = \mathcal{C}_0\exp\left(-(s/2\ell)^2\right). \tag{A4}$$

The variance is defined as

$$\sigma^2 = 2\int_0^L (L-s)\mathcal{C}_2(s)\,\mathrm{d}s = 2\mathcal{C}_0\int_0^L (L-s)\exp\left(-(s/2\ell)^2\right)\mathrm{d}s. \tag{A5}$$

Table B1. Parameters for the data set ($N = 27$) taken from table IV.1 of A. A. Ruzmaikin et al. (1988) using our method (here, like them, we assumed $Gb_0 = 0°$).

Method	$C(s)$	$Gl_0(°)$	$Gb_0(°)$	c_0 (cm^{-3} μG)	ℓ(pc)	$\langle n_e \rangle$ (cm^{-3})	B(μG)
This work	$\mathcal{C}_1$	88 ± 6	0	-0.05 ± 0.004	125	0.06 ± 0.01	1.1 ± 0.1
A. A. Ruzmaikin et al. (1988)	$\mathcal{C}_1$	99 ± 12	0	-0.06 ± 0.002	$100 - 150$	0.035 ± 0.01	2.1 ± 0.5

Splitting the integral:

$$\sigma^2 = 2\mathcal{C}_0 \left[L \int_0^L \exp\left(-(s/2\ell)^2\right) \mathrm{d}s - \int_0^L s \exp\left(-(s/2\ell)^2\right) \mathrm{d}s \right]. \tag{A6}$$

Using standard results for the error function and the exponential integral, we obtain

$$\int_0^L \exp\left(-(s/2\ell)^2\right) \mathrm{d}s = \ell\sqrt{\pi}\ \mathrm{erf}\left(\tfrac{L}{2\ell}\right), \tag{A7}$$

$$\int_0^L s \exp\left(-(s/2\ell)^2\right) \mathrm{d}s = 2\ell^2 \left[1 - \exp\left(-\tfrac{L^2}{4\ell^2}\right)\right]. \tag{A8}$$

Substituting these back gives the final expression for the variance:

$$\sigma^2 = 2\mathcal{C}_0 \left[L\ell\sqrt{\pi}\ \mathrm{erf}\left(\frac{L}{2\ell}\right) - 2\ell^2 \left(1 - \exp\left(-\frac{L^2}{4\ell^2}\right)\right)\right]. \tag{A9}$$

A3 $\mathcal{C}_3$

For $\mathcal{C}_3$, we have

$$\mathcal{C}_3(s) = \mathcal{C}_0 \exp(-s/\ell)\cos(s/\ell). \tag{A10}$$

The variance is defined as

$$\sigma^2 = 2\int_0^L (L - s)\mathcal{C}_3(s)\,\mathrm{d}s$$
$$= 2\mathcal{C}_0 \int_0^L (L - s)\exp(-s/\ell)\cos(s/\ell)\,\mathrm{d}s. \tag{A11}$$

Using standard integration techniques, this integral evaluates to

$$\sigma^2 = \mathcal{C}_0 \left[\ell^2 - \exp(-L/\ell)\Big(\ell^2\cos(L/\ell) + \ell(L\sin(L/\ell) - L\cos(L/\ell))\Big)\right]. \tag{A12}$$

APPENDIX B: RUZMAIKIN ET AL. 1998 DATA

Here, we apply our numerical method to the data in chapter 4 of A. A. Ruzmaikin et al. (1988),which utilized data for 27 pulsars to estimate parameters such as Gl_0, $\langle n_e \rangle$, and B. Note that here we also assume $Gb_0 = 0°$ as they did but in the main text we kept it as a free parameter to be determined from our analysis. The results for both methods are given in Table B1. A key difference in our findings is the value of $\langle n_e \rangle$ (higher than their value) and B (lower than their value) and this may also reflect the numerical approach's ability to capture smaller scale variations that were probably averaged out in their analytical method. In this work, as described and discussed in the main text, we expand the data set to include more than 1200 pulsars and multiple correlation functions (they assumed only the exponential decay, $\mathcal{C}_1$) to provide a more comprehensive analysis of the magneto-ionic medium of the Milky Way.

Table C1. Inferred magneto-ionic medium parameters for the $L_{DM} \leq 20$ kpc sample using different correlation functions ($\mathcal{C}_1, \mathcal{C}_2, \mathcal{C}_3$) under an assumption of non-Gaussian RM and DM distribution with kurtosis, $\kappa = 5$ (see Section 3.5). Uncertainties represent 1σ errors. The table demonstrates that the inferred parameters, including c_0, Gl_0, Gb_0, and ℓ_b remain consistent with the Gaussian case (see Table 1), confirming the robustness of our results against deviations from Gaussianity.

Data set	N	$C(s)$	c_0	$Gl_0(°)$	$Gb_0(°)$	ℓ_b(pc)
$L_{DM} \leq 20$ kpc	1290	$\mathcal{C}_1$	0.05 ± 0.02	192 ± 9	36 ± 33	18 ± 8
$L_{DM} \leq 20$ kpc	1290	$\mathcal{C}_2$	0.05 ± 0.02	192 ± 9	36 ± 33	22 ± 8
$L_{DM} \leq 20$ kpc	1290	$\mathcal{C}_3$	0.05 ± 0.02	192 ± 9	35 ± 34	18 ± 8

Table C2. Similar to Table C2 but for $\langle n_e \rangle$ and $\ell_{\delta n_e}$ using the DM data. These are also consistent with the results assuming Gaussian RM and DM distributions (see Table 2).

Data set	N	$C(s)$	$\langle n_e \rangle$ (cm^{-3})	$\ell_{\delta n_e}$(pc)
$L_{DM} \leq 20$ kpc	3077	$\mathcal{C}_1$	0.055 ± 0.001	251 ± 12
$L_{DM} \leq 20$ kpc	3077	$\mathcal{C}_2$	0.054 ± 0.001	305 ± 12
$L_{DM} \leq 20$ kpc	3077	$\mathcal{C}_3$	0.053 ± 0.001	291 ± 12

APPENDIX C: EFFECT OF NON-GAUSSIANITY IN RM AND DM DISTRIBUTIONS

To assess the sensitivity of our results to the assumption of Gaussian probability density functions (PDFs) for RM and DM (via the choice of distribution for ϵ_{RM} in equation 22 and η_{DM} in equation 38), we generated non-Gaussian distributions as described in Section 3.5. For both RM and DM, we tested a range of kurtosis values, $\kappa = 0, 0.1, 1, 2, 5$, for the full sample and for representative subsamples (data sets in Tables 1 and 2). Tables C1 and C2 illustrates the case with the highest kurtosis, $\kappa = 5$, representing the most extreme departure from Gaussianity.

We find that all the inferred parameters are statistically indistinguishable from those obtained under the Gaussian assumption. Across all tested distributions, the inferred magnetic field and thermal electron density remain consistent with the Gaussian case within uncertainties, suggesting that the results are determined mainly by the central part of the distributions rather than the tails. These results demonstrate that our conclusions are robust against deviations from Gaussianity, and that the low values of the reduced χ^2 discussed in Section 2.4 are unlikely to result solely from the assumption of Gaussian PDFs.

This paper has been typeset from a TEX/LATEX file prepared by the author.